Title
First-Principles Investigation of Core Level Second Harmonic Generation as Interfacial Probe

Author
Jamnuch, Sasawat

Publication Date
2023

Peer reviewed|Thesis/dissertation

UNIVERSITY OF CALIFORNIA SAN DIEGO

First-Principles Investigation of Core Level Second Harmonic Generation as Interfacial Probe

A Dissertation submitted in partial satisfaction of the requirements
for the degree Doctor of Philosophy

in

Chemical Engineering

by

Sasawat Jamnuch

Committee in charge:

Professor Tod Pascal, Chair
Professor David Fenning
Professor Alex Frano
Professor Shyue Ping Ong
Professor Wei Xiong

2023

The Dissertation of Sasawat Jamnuch is approved, and it is acceptable in quality and form for publication on microfilm and electronically.

University of California San Diego

2023

TABLE OF CONTENTS

LIST OF FIGURES

LIST OF ABBREVIATIONS

BSE	Bethe-Salpeter Equation
B-PN	Boron-Parylene-N
B-V	Boron-Vacuum
DFT	Density functional theory
DOS	Density of states
LCO	Lithium cobalt oxide
LLTO	Lithium lanthanum titanate
LTO	Lanthanum titanium oxide
PAW	Projector augmented wave
SCF	Self-consistent field
RT-TDFFT	Real-time time-dependent density functional theory
TDDFT	Time-dependent density functional theory
TDKS	Time-dependent Kohn-Sham
SH	Second harmonic
SHG	Second harmonic generation
SXR	Soft X-ray
vDOS	Vibrational density of states
XAS	X-ray absorption spectroscopy
XFEL	X-ray free electron laser
XUV	Extreme ultraviolet

ACKNOWLEDGEMENTS

I would like to acknowledge my entire committee for their time, feedback and support for my research especially my advisor Professor Tod Pascal. Tod has been an immense help and enthusiastic supporter for my research. His advice was very helpful throughout my Ph.D. study both in life and work.

I would like to acknowledge my experimentalist collaborators Sumana Raj, Tobias Helk, Emma Berger, Can Uzundal, Craig Schwartz, Walter Drisdell and Michael Zuerch for all our fruitful work together.

I would like to also acknowledge Das Pemmaruju, David Prendergast and Subhayan Roychodhury for their mentorship on the simulation codes and broad discussion on scientific work.

I would also like to acknowledge my labmates Amanda Chen, Pedram Abbasi, Alexandria Do, Robert Ramji and Ricardo Silva-buarque for their friendship and scientific discussion.

I would also like to acknowledge Thai students' community in San Diego for their friendship. It has truly been a pleasure and made my life in the states much more enjoyable and memorable.

Lastly, I would like to acknowledge my parents for their love, support and encouragement for my study throughout my Ph.D. I would never have made it this far without their support and love.

Chapter 2, in full, is a reprint of the material as it appears in *Nano Letters* **2021** *21* (14), 6095-6101. Emma Berger, Sasawat Jamnuch, Can B. Uzundal, Clarisse Woodahl, Hari

Padmanabhan, Angelique Amado, Paul Manset, Yasuyuki Hirata, Yuya Kubota, Shigeki Owada, Kensuke Tono, Makina Yabashi, Cuixiang Wang, Youguo Shi, Venkatraman Gopalan, Craig P. Schwartz, Walter S. Drisdell, Iwao Matsuda, John W. Freeland, Tod A. Pascal, and Michael Zuerch. The dissertation author was the primary investigator of the theoretical part and author of this paper. Emma Berger and Sasawat Jamnuch have equal contributions to the work.

Chapter 3, in full, is a reprint of the material as it appears in Phys. Rev. Lett. 127, 096801, Craig P. Schwartz, Sumana L. Raj, Sasawat Jamnuch, Chris J. Hull, Paolo Miotti, Royce K. Lam, Dennis Nordlund, Can B. Uzundal, Chaitanya Das Pemmaraju, Riccardo Mincigrucci, Laura Foglia, Alberto Simoncig, Marcello Coreno, Claudio Masciovecchio, Luca Giannessi, Luca Poletto, Emiliano Principi, Michael Zuerch, Tod A. Pascal, Walter S. Drisdell, and Richard J. Saykally. The dissertation author was the primary investigator of the theoretical part and author of this paper. Craig P. Schwartz, Sumana L. Raj and Sasawat Jamnuch have equal contributions to the work.

Chapter 4, in full, is a reprint of the material submitted to Nat. Mat. with the following authors Clarisse Woodahl, Sasawat Jamnuch, Angelique Amado, Can B. Uzundal, Emma Berger, Paul Manset, Yisi Zhu, Yan Li, Dillon D. Fong, Justin G. Connell, Yasuyuki Hirata, Yuya Kubota, Shigeki Owada, Kensuke Tono, Makina Yabashi, Sanja Tepavcevic, Iwao Matsuda, Walter S. Drisdell, Craig P. Schwartz, John W. Freeland, Tod A. Pascal, Alfred Zong, Michael Zuerch. The dissertation author was the primary investigator of the theoretical part and author of this paper. Clarisse Woodahl and Sasawat Jamnuch have equal contributions to the work.

VITA

2014 Bachelor of Chemical Engineering, Thammasat University, Thailand

2018 Master of Science in Chemical Engineering, University of California San Diego

2023 Doctor of Philosophy in Chemical Engineering, University of California San Diego

ABSTRACT OF THE DISSERTATION

First-Principles Investigation of Core Level Second Harmonic Generation as Interfacial Probe

by

Sasawat Jamnuch

Doctor of Philosophy in Chemical Engineering

University of California San Diego, 2023

Professor Tod Pascal, Chair

Interfacial probe at elemental selectivity is highly sought after experimental tool. Chemical phenomena happen at the interface and our understanding these processes is often challenging. Second harmonic generation (SHG) spectroscopy technique can selectively probe the interface due to symmetry breaking. Coupling this technique with core electron XUV/X-ray spectroscopy allows elemental selectivity. In this regard, the development of novel core level second harmonic generation spectroscopy demonstrates a powerful tool at

atomic resolution.

Theoretical framework for simulation of XUV/X-ray SHG is developed to study different interfaces and interpret the experimental result. In this research, we explored Li ion displacement in ferroelectric perovskite $LiOsO_3$ is studied via XUV-SHG, boron electronics structure at inorganic/organic junction and Li mobility in solid-state electrolyte lithium lanthanum titanate. In all cases, the bulk responses were indistinguishable between different interfaces while the surface sensitive SHG technique demonstrate different responses. Our approach shows a promising result toward elemental selective interfacial probe.

CHAPTER 1

INTRODUCTION

Interfaces are what separate material from another. Most chemical processes occur at the interface. It is challenging to probe these interfaces especially at atomic resolution. Therefore, it is crucial that one employed high selectivity method to study interfacial process. A key aspect of this research focuses on theoretical development and interpretation of experimental data. This thesis is therefore a focus on theoretical application and interpretation to real complex interfaces involving different phenomena such as electrochemical catalysis and ion diffusion.

1.1. Atomic Scale Resolution

Atomic theory has gone a long way starting from a philosophical point of view as a description of nature and matter. Over the course of human history, the atomic theory slowly combines elements of physics, chemistry and mathematics leading to modern description of modern day[1,2].

The word “atom” comes from ancient Greek word *atomos* which means indivisible. The idea of atomism believes that matter consists of discrete particles which are indestructible and indivisible units called atoms[3]. What we normally observed is hence a statistical average of these miniscule particles acting together. It took until the end of 18th century for the first scientific version of atom was truly developed and supplied with experimental evidence. The first version is commonly known as Dalton’s atomic theory where he proposed that each chemical element consists of a single type of identical atom that persists through any chemical means[4]. Over the next two centuries, we see inclusion of quantum mechanics into the atom theory leading to modern version of atom.

Modern day theoretical atoms are tiny particles made up from subatomic particles;

neutron, proton, and electron[5]. The key result from quantum mechanics inclusion to atomic theory led to the Schrodinger equation which is a governing equation for wave function of a quantum-mechanical system[6].

The resolution of atom is in the range of angstrom (10^{-10} m) and phenomena happened at this scale is often ultrafast (< 10^{-15} s)[7,8]. This proves to be a significant challenge at trying to understand any process at this scale. Looking through the lens, Antoine van Leeuenhoek of Holland created a microscope which allowed the discovery of microorganisms[9]. The more complex version was developed by Robert Hooke with higher magnification[10]. He coined his discovery the biological term cell. Despite this discovery, the size of a cell is on a micron scale (~10^{-6} m) which is far off from the size of atom. Various observation methods and tools were invented to improve the resolution of the microscope but in the end a limit resolution is reached due to the nature of light[11]. It becomes apparent that if we really want to see things at atomic scale resolution, we are required to use probing light at the same length scale.

The discovery of X-rays and electron in 19th century resulted in the development of electron microscopes[12-14]. Electron microscopes surpass the limitation of optical light and for the first time allow us a step closer to observe objects such as atomic nuclei. However, with the advent of quantum theory, it is prohibited to observe the position and momentum of quantum object (which atoms and all its subatomic particles are) with absolute precision. While the truth is discouraging, it is still possible to indirectly see and extract information at atomic scale level. This understanding is the foundation of most modern measurement apparatus[15].

From what has been discussed above, it becomes apparent that atomic scale resolution is

extremely challenging to reach and observation of phenomena at the scale requires something of similar length and time scale. In addition, the interpretation of these experiment is difficult. Therefore, theoretical investigation is mandatory to truly understand the underlying factors or driving force in the phenomena of interest.

1.2. Density Functional Theory

Our understanding of atoms and chemical bonding leads us to the main actor in all matter, electron. It becomes apparent that to extract information at atomic scale, electrons must be probed through different means. Similarly, once one properly modeled and obtained accurately the picture and description of electrons in the system of interest, one may extract any relevant information of interest. The challenge in theory and modeling part however is due to original Schrodinger equation formalism. The governing equation is limited to very small system, only hydrogen or helium can be solved exactly. Thus, it is not applicable to any real system. Paul Dirac summed the situation perfectly in 1929, "The underlying physical laws necessary for the mathematical theory of a large part of physics and the whole of chemistry are thus completely know, and the difficulty is only that the exact application of these laws leads to equations much too complicated to be soluble."[16]. Significant developments into the quantum chemistry and physics slowly have since been made to surpass this limitation toward general application. Notably in 1965, Walter Kohn and Lu Jeu Sham introduced the concept of density functional theory (DFT)[17]. Their work has laid a foundation on the computational chemistry as their framework allows modeling of any chemical system of interest[18].

Firstly, the nuclei have much more mass than the electrons thus moving much more

slowly. The large disparity between nuclear and electronic motion can be utilized to our advantage by considering the nuclear motion as decoupled from the electronic motion. This is the so called Born-Oppenheimer approximation. In practice, the interacting electrons and nuclei can be modeled with frozen nuclei.

The Kohn-Sham equation is given in a form of

$$\left(-\frac{\bar{h}^2}{2m}\nabla^2 + v_{eff}(r)\right)\varphi_i(r) = \varepsilon_i\varphi_i(r).$$

The eigenvalue equation above typically represents Kohn-Sham equations. Here. ε_i is the orbital energy corresponding to the Kohn-Sham orbital φ_i and the density of the entire system of N-particle is given by

$$\rho(r) = \sum_i^N |\varphi_i(r)|^2.$$

The advantage of DFT is that it effectively reduce the many-body problem of N electrons with 3N spatial coordinates into single unified electron density given by a single three spatial coordinates. The electron density and its interaction are approximated using functionals. Hence, DFT is the first step toward accessing material property. While standard DFT calculation is groundstate theory meaning it does not allow access to excited state of the system, the solution from DFT calculation still serves as a starting point toward excited state calculation[19].

To summarize, DFT is now commonly used first-principle tool for studying any chemical system. The solutions from DFT are used in further calculation to access desired properties.

1.3. X-ray and Excited State

X-ray techniques have evolved significantly over decades to become highly specialized

tool for a broad range of investigations[20]. These techniques rely on interaction between high energy X-ray photon and electrons of the probed material. As dictated by quantum mechanics, the energies of electron are quantized and generally distinguishable between different elements[21]. Consequently, the interaction between X-ray and electron needed to be commensurate. By using properly tuned X-ray energy pulse, one may illicit response with high selectivity in contrast to optical regime where electronic response is usually collective response of entire material[22]. This paves way toward greater understanding of any chemical phenomena at atomic scale as the timescale and length scale of this interaction can be tuned. Traditionally, X-ray measurements depend on the number of incident X-ray photons. Recent advent of X-ray free electron lasers (XFELs) has opened our ability to create high photon numbers with ultrashort X-ray pulse[23,24]. This enables us to study phenomena at ultrafast timescale such as charge transfer, phase transition or catalysis.

Excitation from X-ray pulse leads to core-level excitation where the core electrons with matching energy are excited. Different X-ray spectroscopy techniques are used to study local structure and electronic state of matter. Excitation process can vary depending on where the excited electron ends up as shown in Figure 1.1. In addition, non-linear process can also take place involving more than single photon and/or electron.

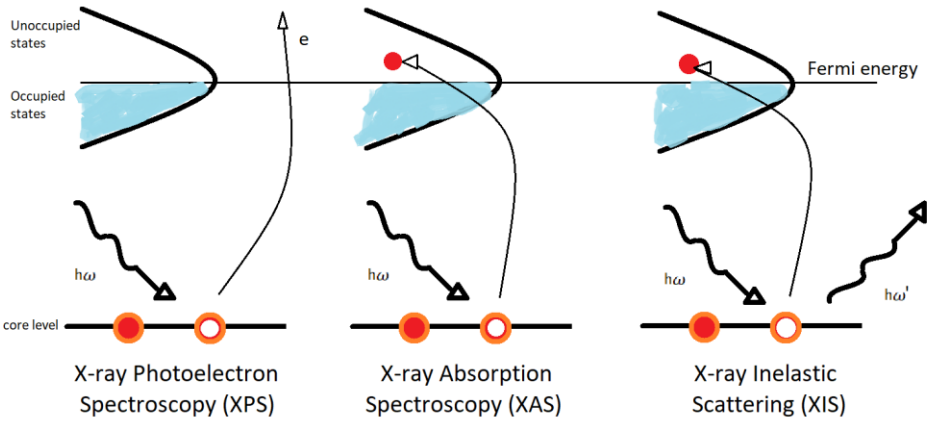

Figure 1.1. Conventional X-ray technique.

Interpretation of X-ray measurements become increasing challenging as it is now possible to study real complex and functional material[25].While it is possible to resolve the excitation of simple gas or small molecule, excitation in solid-state is often more complex[26]. Therefore, an investigation from first-principle study is commonly required to truly understand the underlying factors in X-ray study. The response of X-ray excitation of any material can be computed using the solution from DFT groundstate calculation[27]. One of the most common ways to access the excited states is through time-dependent density functional theory (TDDFT).

In short, X-ray measurements allow us to selectively probe material at atomic resolution. Recent developments from XFELs and experimental techniques have started a new road for material study and exploration, but interpretation of these experimental results cannot be completed without using theoretical simulation.

1.4. Interface probe technique

Interface between two bulk phases is where many chemical processes occur. Examples of interface includes water/oil, vapor/liquid, solid/aqueous interfaces, grain boundary

and biological membrane. We often find that the behaviors of the matter at the interface are notably different than the bulk. To illustrate, water density profile at solid/aqueous interface phase is different than the bulk due to interaction between water molecules at the wet surface[28]. Additionally, adsorption process where chemical is attached to the surface plays a major role in facilitating catalysis[29]. Thus. The important component of chemistry greatly involves interface.

To further our understanding, experimental insights with information solely from the interface or surface are desirable. Understanding matter behavior at atomic scale not limited to just adsorption/desorption, kinetic and dynamics is primary objective toward better material engineering.

Characterization through X-ray spectroscopy provides understanding of electronic structure at atomic scale along with the local environment. X-ray spectroscopy is powerful in this aspect as the technique is possible to qualitatively assessed defect level at low concentration order of 0.1% in semiconductor[30]. The application of X-ray spectroscopy can be extended to study the reacting catalytic surface [https://doi.org/10.1021/acs.chemrev.0c00396].

More advanced technique for probing only the interface requires nonlinear process[31,32]. The most common approach is to use second harmonic generation (SHG). Second harmonic generation is a coherent second order nonlinear process where two photons of the same energy are simultaneously absorbed, and the system relaxes by releasing a single photon with double the frequency. The process has been used extensively to study surfaces on centrosymmetry materials due to the electric-dipole contribution from SHG from the bulk is zero due to symmetry consideration[33]. Therefore, the majority of the

signal arises from the interface or surface where centrosymmetry is broken.

Second harmonic generation was first implemented with optical light for biological imaging. However, its idea can be extended into X-ray regime to study electronic structure at the interface to the atomic scale. Hence, by combining the elemental selectivity and atomic scale resolution of X-ray and surface/interface selectivity of SHG techniques, we can have a highly selective interfacial probe at atomic level.

To compensate for these experimental advents, theoretical framework for accurate simulation of linear and nonlinear response is of great need. While there are multiple approaches for simulating linear X-ray response, the nonlinear or time resolved response theoretical framework is limited. A well-established theoretical method for simulating atomic scale response from interface would be beneficial to further our understanding.

1.5. Theoretical approaches for X-ray responses simulation.

There are multiple first-principle methods to simulate X-ray response. Here, this chapter focuses only on the methods employed in this dissertation. In modeling the X-ray response from the simulation, we consider the response of the system total polarization (P) to an arbitrary external field (E)[34]. The polarization can be expanded as a function of electric field component E_i.

$$P_i = P_i^0 + \chi_{ij}^{(1)} E_j + \chi_{ijk}^{(2)} E_j E_k + \cdots$$

Here , *i, j, k* denote the x, y, z direction along the Cartesian axes. P_i is the total induced polarization. P^0 is the permanent polarization. $\chi_{ij}^{(1)}$ and $\chi_{ijk}^{(2)}$ are the linear polarizability and second-order polarizability. The linear polarizability is the quantity related to electron X-ray interaction from X-ray absorption experiment while the second-order

polarizability relates to the second order processes such as sum frequency generation or second harmonic generation.

1.5.1. Simulation of linear response in frequency domain using Many-Body Perturbation Theory

The linear X-ray absorption intensity is proportional to the probability of electronic transition between the initial state φ_i and the final state φ_f [35,36]. In general, the transition between φ_i and φ_f due to excitation from photon incoming energy ω is given by the *Fermi Golden Rule*:

$$\Gamma_{i\to f} = \frac{2\pi}{\bar{h}} |< \varphi_i | \bar{V} | \varphi_f >|^2 \delta(\varepsilon_i - \varepsilon_f + \bar{h}\omega)$$

where $\bar{V}$ is the operator describing the interaction between radiation and matter, ε_i and ε_f are the electron energies in the initial and final states. Within the dipole approximation, the transition matrix ($\mathbf{d_{fi}}$) is simplified to

$$\mathrm{d}_{fi} = |< \varphi_i | \hat{\epsilon} \cdot r | \varphi_f >|$$

where $\hat{\epsilon}$ and r are the photon polarization and position operator.

The X-ray absorbance $\sigma(\omega)$ correlating between experimental spectra and first principles model can be related from

$$\sigma(\omega) \propto \omega \sum_f |< \varphi_i | \hat{\epsilon} \cdot r | \varphi_f >|^2 \delta(\varepsilon_i - \varepsilon_f + \bar{h}\omega)$$

Liang et al. pioneered the Many-body X-ray Absorption Spectroscopy (MBXAS) approach based on Slater determinant comprising of noninteracting Kohn-Sham orbitals[37]. The initial state ($|\varphi_i >$) independent KS orbitals are obtained from ground state DFT calculation. To access the final excited states, constrained occupancy DFT or the Delta self-consistent field (ΔSCF) approach is used. This method represents the excited state due to X-ray excitation by removing the excited

electron from the excited atom and performing the DFT calculation. For example, carbon K-edge excitation is simulated from pseudopotential generated with $1s^1$ configuration. A supercell with size of (> 10 Å) is needed to avoid interaction between artificial periodic images. The advantage of this approach is that it allows one to study larger system such as system with site vacancy or defect. In addition, the accuracy is greatly improved showing comparable result to Bethe-Salpeter equation (BSE) approach.

1.5.2. Simulation of linear Response from real-time velocity gauge time dependent density functional theory (RT-TDDFT)

The velocity-gauge form of equation is suitable for infinite periodic systems and obtained by a gauge transformation of time dependent KS equation. This formalism is the extension of length-gauge formalism which has been shown to model molecular system accurately[38]. The time-dependent Kohn-Sham equation (TDKS) is given by[39]:

$$i\bar{h}\frac{\partial}{\partial t}\varphi_i(r,t) = \hat{H}_{KS}\varphi_i(r,t).$$

with the velocity-gauge Hamiltonian $\hat{H}_{KS}$ given by:

$$\hat{H}_{KS} = \left\{\frac{1}{2m}[\vec{p} + \frac{e}{c}\vec{A}(t)]^2 + \hat{V}_{ion} + \int d\vec{r}\frac{e^2}{|\vec{r}' - \vec{r}|}\rho(r) + V_{xc}\rho(r)\right\}$$

Here, $\vec{A}(t)$ is the applied electrical field which is an impulse function to illicit linear response. Integrating the TDKS yields the time-dependent electron density and the time-dependent current.

$$\vec{I}(t) = -\frac{e}{\Omega}\int_{\Omega} dr\vec{j}(r,t)\,.$$

The frequency domain quantities can then be accessed through Fourier transformation of the time dependent current to yield the frequency dependent conductivity

$$\sigma_{ij}(\omega) = -\frac{c}{A_{0j}}\int^{T} dt exp(i\omega t) I_i(t)$$

and the frequency dependent dielectric function

$$\varepsilon_{ij}(\omega) = 1 + \frac{4\pi i \sigma_{ij}(\omega)}{\omega}$$

While this formalism is generalized for all the systems, extraction of core electron's response requires inclusion of the core electron into the pseudopotential. For example, carbon 1s electrons have to be included into the simulation for C K-edge simulation. The benefit of solving TDDFT is that the excited states are accurately modeled and evolved with the system. It also allows study of ultrafast real-time phenomena otherwise not accessible with frequency domain method.

1.5.3. **Simulation of second-order susceptibility in frequency domain**

Calculation of second-order susceptibility tensor of second harmonic generation, the formalism from Sharma et al.[40] is employed. Within this formalism, the second-order susceptibility $\chi^2(2\omega, \omega, \omega)$ is contributed by the excitation energies resonant at ω and 2ω. In general, the second-order susceptibility is given by

$$\chi^{(2)}_{ijk}(2\omega,\omega,\omega) = \frac{1}{\Omega}\sum_{ff'}\left(\frac{\langle i\rangle_{gf}\langle j\rangle_{ff'}\langle k\rangle_{f'g}}{(\omega_{fg}-2\omega)(\omega_{f'g}-\omega)} + \frac{\langle j\rangle_{gf}\langle i\rangle_{ff'}\langle k\rangle_{f'g}}{(\omega_{fg}+\omega)(\omega_{f'g}-\omega)} + \frac{\langle j\rangle_{gf}\langle k\rangle_{ff'}\langle i\rangle_{f'g}}{(\omega_{fg}+\omega)(\omega_{f'g}+2\omega)}\right)$$

where *g,f,f'* represent the groundstate, intermediate state and final state respectively. For core electron response, special treatment is required to remove numerical noise at high energy as the density of states at this excitation leads to noisy response[41]. The lifetime broadening is added as imaginary part to the Kohn-Sham eigenenergies

to smooth out the densities of state and reduce numerical noise.

$$\varepsilon_m = \varepsilon_m + \frac{i}{\lambda}\sqrt{\varepsilon_m - E_F}$$

Where ε_m is the Kohn-Sham energy, λ is the inelastic mean free path of electrons and E_F is the fermi energy.

To extract second harmonic response, the simulation cell is commonly setup as a junction between two interested interfaces. This is the origin of the response as it is where the symmetry is broken. For vacuum/solid interface, one commonly employed a simulation trick where the symmetry is artificially broken by only including the first few top layers of material with core electron while the rest of the slab only contains the valence electron in the calculation. Lastly, the bands included in the calculation are chosen such that only the core electron response of interest is extracted.

1.5.4. Simulation of second-order susceptibility using real-time time dependent density functional theory (RT-TDDFT)

Following the methodology established in section 1.5.2., the nonlinear response due to excitation at ω can be simulated. However, the calculation of frequency-dependent nonlinear polarizabilities is more complicated than the linear response. In particular, the nonlinear response functions are convoluted with the external field $\vec{A}$ (t) and all the components cannot be obtained by simply applying the impulse function only once. In practice, pure delta function will require an infinite simulation time to fully extract nonlinear response from the system. Thus, in order to simulate the nonlinear response, a monochromatic wave-packet generally sinusoidal or Gaussian of frequency ω is used for the applied field. The perk of this

approach also allows in silico simulation of real-world experiment where light and matter interact. The nonlinear response can then be extracted for the higher order response at n^{th} ω from Fourier transformation of the time-dependent current similar to how one obtains the linear response.

Simulation of second-order response can be done by performing calculation using perturbed wave-packet at ω with varying field strength. As this is the second-order process, the corresponding strength of the Fourier transformed time-dependent current will be quadratic and the second-order susceptibility $\chi^2(2\omega, \omega, \omega)$ is proportional coefficient of the second order term from the relation between field strength (E) and the frequency-dependent current I(2ω).

The simulation setup for this approach is also identical to section 1.5.3. in that it requires symmetry breaking along the polarization direction to simulate second-harmonic response from the system of interest.

1.6. Dissertation Contents

The primary focus of this research describes in the following chapters is the development and application of theoretical investigation of X-ray second harmonic generation for interfacial probe. The main objectives are to give a better understanding and interpretation of experimental results. Chapter 2 describes the second-harmonic generation in XUV regime of lithium ions in polar metal $LiOsO_3$. The polar metal $LiOsO_3$ is a prime candidate to investigate the second-harmonic generation at core level as $LiOsO_3$ is polar at low temperature phase due to Li displacement along the polar axis leading to symmetry breaking. By employing second harmonic generation technique at Li K-edge, the Li response can be selectively probe and was found to be distinct

depending on the displacement along the polar axis.

Chapter 3 describes the second-harmonic generation at soft X-ray regime at buried inorganic-organic junction. Here, the boron K-edge representing prototype inorganic material and polymer representing organic material are probed. The boron/vacuum and boron/polymer interfaces are shown to be indistinguishable using linear XAS. However, second-harmonic response differs and is shown to be dependent on the distance between polymer and boron at the junction. This paves way toward highly precise atomic scale buried interface probe.

Chapter 4 describes the second-harmonic generation at XUV of Li K-edge in Lithium Lanthanum Titanate (LLTO) which is a prototype solid electrolyte. The Li K-edge second-harmonic response is used to probe the electronic structure of Li at the interface. The Li mobility is found to be lower at the interface with vibrational modes being absent at the interface. This demonstrates that the interface of solid electrolyte is crucial for battery performance. In addition, our second-harmonic generation approach is powerful method at investigating material properties at the interface.

The dissertation concludes with a conclusion chapter 5 summarizing all the works from chapter 2 to 4 along with future development prospect for theoretical framework and venue to explore in experimental area.

1.7. Chapter 1 References

1 Constable, E. C. & Housecroft, C. E. Chemical Bonding: The Journey from Miniature Hooks to Density Functional Theory. *Molecules* 25, doi:10.3390/molecules25112623 (2020).

2 Clarke, F. W. The Atomic Theory. *Science* **18**, 513-529, doi:10.1126/science.18.460.513 (1903).

3 Berryman, S. Ancient Atomism. *The Stanford Encyclopedia of Philosophy. Metaphysics Research Lab, Stanford University* **Winter 2022** (2022).

4 Rocke, A. J. In Search of El Dorado: John Dalton and the Origins of the Atomic Theory. *Social Research: An International Quarterly* **72**, 125-158, doi:10.1353/sor.2005.0003 (2005).

5 Zuidgeest, M. The concept of matter in modern atomic theory. *Acta Biotheoretica* **26**, 30-38, doi:10.1007/bf00115925 (1977).

6 Schrödinger, E. An Undulatory Theory of the Mechanics of Atoms and Molecules. *Physical Review* **28**, 1049-1070, doi:10.1103/PhysRev.28.1049 (1926).

7 Smith, D. J. Progress & perspectives for atomic-resolution electron microscopy. *Materials Today* **12**, 10-16, doi:10.1016/s1369-7021(10)70140-1 (2010).

8 Elsaesser, T. Introduction: Ultrafast Processes in Chemistry. *Chem Rev* **117**, 10621-10622, doi:10.1021/acs.chemrev.7b00226 (2017).

9 van Zuylen, J. The microscopes of Antoni van Leeuwenhoek. *J Microsc* **121**, 309-328, doi:10.1111/j.1365-2818.1981.tb01227.x (1981).

10 Ash, C. Hooke's microscope. *Trends in Microbiology* **6**, doi:10.1016/s0966-842x(98)01380-8 (1998).

11 Thorn, K. A quick guide to light microscopy in cell biology. *Mol Biol Cell* **27**, 219-222, doi:10.1091/mbc.E15-02-0088 (2016).

12 Assmus, A. Early History of X Rays

13 Behling, R. X-ray sources: 125 years of developments of this intriguing technology. *Phys Med* **79**, 162-187, doi:10.1016/j.ejmp.2020.07.021 (2020).

14 Rudenberg, H. G. & Rudenberg, P. G. in *Advances in Imaging and Electron Physics* Vol. 160 207-286 (Elsevier, 2010).

15 Castner, E. W. Modern Spectroscopy, 4th Edition (J. Michael Hollas). *Journal of Chemical Education* **82**, doi:10.1021/ed082p43.1 (2005).

16 Simões, A. Dirac's Claim and the Chemists. *Physics in Perspective* **4**, 253-266, doi:10.1007/s00016-002-8369-1 (2002).

17 Kohn, W. & Sham, L. J. Self-Consistent Equations Including Exchange and Correlation Effects. *Physical Review* **140**, A1133-A1138, doi:10.1103/PhysRev.140.A1133 (1965).

18 Mardirossian, N. & Head-Gordon, M. Thirty years of density functional theory in computational chemistry: an overview and extensive assessment of 200 density functionals. *Molecular Physics* **115**, 2315-2372, doi:10.1080/00268976.2017.1333644 (2017).

19 Adamo, C. & Jacquemin, D. The calculations of excited-state properties with Time-Dependent Density Functional Theory. *Chem Soc Rev* **42**, 845-856, doi:10.1039/c2cs35394f (2013).

20 Malzer, W., Schlesiger, C. & Kanngießer, B. A century of laboratory X-ray absorption spectroscopy – A review and an optimistic outlook. *Spectrochimica Acta Part B: Atomic Spectroscopy* **177**, doi:10.1016/j.sab.2021.106101 (2021).

21 Zimmermann, P. *et al.* Modern X-ray spectroscopy: XAS and XES in the laboratory. *Coordination Chemistry Reviews* **423**, doi:10.1016/j.ccr.2020.213466 (2020).

22 Henderson, G. S., de Groot, F. M. F. & Moulton, B. J. A. X-ray Absorption Near-Edge Structure (XANES) Spectroscopy. *Reviews in Mineralogy and Geochemistry* **78**, 75-138, doi:10.2138/rmg.2014.78.3 (2014).

23 Pellegrini, C. The development of XFELs. *Nature Reviews Physics* **2**, 330-331, doi:10.1038/s42254-020-0197-1 (2020).

24 Bencivenga, F. *et al.* Nonlinear optics with coherent free electron lasers. *Physica Scripta* **T169**, doi:10.1088/0031-8949/t169/1/014003 (2016).

25 Rehr, J. J. & Ankudinov, A. L. Progress and challenges in the theory and interpretation of X-ray spectra. *J Synchrotron Radiat* **8**, 61-65, doi:10.1107/s0909049500016423 (2001).

26 Cutsail Iii, G. E. & DeBeer, S. Challenges and Opportunities for Applications of Advanced X-ray Spectroscopy in Catalysis Research. *ACS Catalysis*, 5864-5886, doi:10.1021/acscatal.2c01016 (2022).

27 Norman, P. & Dreuw, A. Simulating X-ray Spectroscopies and Calculating Core-Excited States of Molecules. *Chem Rev* **118**, 7208-7248, doi:10.1021/acs.chemrev.8b00156 (2018).

28 Gim, S., Cho, K. J., Lim, H. K. & Kim, H. Structure, Dynamics, and Wettability of Water at Metal Interfaces. *Sci Rep* **9**, 14805, doi:10.1038/s41598-019-51323-5 (2019).

29 Somorjai, G. A. & Li, Y. Impact of surface chemistry. *Proc Natl Acad Sci U S A* **108**, 917-924, doi:10.1073/pnas.1006669107 (2011).

30 Huber, S. P. *et al.* Detection of defect populations in superhard semiconductor boron subphosphide B12P2 through X-ray absorption spectroscopy. *Journal of Materials Chemistry A* **5**, 5737-5749, doi:10.1039/c6ta10935g (2017).

31 Watts, K. E., Blackburn, T. J. & Pemberton, J. E. Optical Spectroscopy of Surfaces, Interfaces, and Thin Films: A Status Report. *Anal Chem* **91**, 4235-4265, doi:10.1021/acs.analchem.9b00735 (2019).

32 Johansson, P. K., Schmuser, L. & Castner, D. G. Nonlinear Optical Methods for Characterization of Molecular Structure and Surface Chemistry. *Top Catal* **61**, 1101-1124, doi:10.1007/s11244-018-0924-3 (2018).

33 Schneider, L. & Peukert, W. Second Harmonic Generation Spectroscopy as a Method for In Situ and Online Characterization of Particle Surface Properties. *Particle & Particle Systems Characterization* **23**, 351-359, doi:10.1002/ppsc.200601084 (2006).

34 Hertel, P. Lectures on Theoretical Physics Linear Response Theory

35 Hetenyi, B., De Angelis, F., Giannozzi, P. & Car, R. Calculation of near-edge x-ray-absorption fine structure at finite temperatures: spectral signatures of hydrogen bond breaking in liquid water. *J Chem Phys* **120**, 8632-8637, doi:10.1063/1.1703526 (2004).

36 Taillefumier, M., Cabaret, D., Flank, A.-M. & Mauri, F. X-ray absorption near-edge structure calculations with the pseudopotentials: Application to theKedge in diamond andα-quartz. *Physical Review B* **66**, doi:10.1103/PhysRevB.66.195107 (2002).

37 Liang, Y. *et al.* Accurate X-Ray Spectral Predictions: An Advanced Self-Consistent-Field Approach Inspired by Many-Body Perturbation Theory. *Phys Rev Lett* **118**, 096402, doi:10.1103/PhysRevLett.118.096402 (2017).

38 Takimoto, Y., Vila, F. D. & Rehr, J. J. Real-time time-dependent density functional theory approach for frequency-dependent nonlinear optical response in photonic molecules. *J Chem Phys* **127**, 154114, doi:10.1063/1.2790014 (2007).

39 Yabana, K., Sugiyama, T., Shinohara, Y., Otobe, T. & Bertsch, G. F. Time-dependent density functional theory for strong electromagnetic fields in crystalline solids. *Physical Review B* **85**, doi:10.1103/PhysRevB.85.045134 (2012).

40 Sharma, S. & Ambrosch-Draxl, C. Second-Harmonic Optical Response from First Principles. *Physica Scripta* **T109**, doi:10.1238/Physica.Topical.109a00128 (2004).

41 Lam, R. K. *et al.* Soft X-Ray Second Harmonic Generation as an Interfacial Probe. *Phys Rev Lett* **120**, 023901, doi:10.1103/PhysRevLett.120.023901 (2018).

CHAPTER 2

Extreme Ultraviolet Second Harmonic Generation Spectroscopy in a Polar Metal

2.0. Abstract

The coexistence of ferroelectricity and metallicity seems para-doxical, since the itinerant electrons in metals should screen the long-range dipole interactions necessary for dipole ordering. The recent discovery of the polar metalLiOsO3 was therefore surprising [as discussed earlier in Y. Shi et al., Nat. Mater.2013, 12, 1024]. It is thought that the coordination preferences of the Li play a key role in stabilizing the LiOsO3 polar metal phase, but an investigation from the combined viewpoints of core-state specificity and symmetry has yet to be done. Here, apply the novel technique of extreme ultraviolet second harmonic generation (XUV-SHG) and find a sensitivity to the broken inversion symmetry in the polar metal phase of $LiOsO_3$ with an enhanced feature above the Li K-edge that reflects the degree of Li atom displacement as corroborated by density functional theory calculations. These results pave the way for time-resolved probing of symmetry-breaking structural phase transitions on femtosecond time scales with element specificity.

2.1. Introduction

A central question of condensed matter physics is how the structure of a material gives rise to its function. One approach to this so-called “structure−function problem” is to ask how the elemental composition plays a role in a material’s emergent functionality. A symmetry-based perspective offers yet another valuable viewpoint. Here, we combine the insights of both approaches in a single experiment, namely extreme ultraviolet second harmonic generation (XUV-SHG), to explore the nonintuitive coexistence of

polarity and metallicity in $LiOsO_3$. Although it was first predicted over 50 years ago that polar metals could form through a second-order phase transition, the first experimentally realized "ferroelectric-like" metal, lithium osmate ($LiOsO_3$), was discovered only recently.[1,2] The search for polar metals has since expanded, motivated by prospects of multiferroics,[3] electrodes in ferroelectric nanocapacitors,[4] nonlinear optical media,[5] polar superconductors,[6–8] and thermoelectric devices.[9] Recent works predicting asymmetric hysteresis in $LiOsO_3$ thin films and revealing ferroelectric switching in a two-dimensional metal[10] have generated significant recent excitement for the practical application of low-dimensional devices. Despite the numerous attempts to explain the coexistence of polarity and metallicity, there are still many unanswered questions as to how polar order can be stabilized in a metal.

Since its discovery, $LiOsO_3$ has become a prototypical polar metal. In this perovskite-structured material (ABO_3), a continuous order−disorder phase transition occurs at a critical temperature of T_c = 140 K, where it transitions from an $\overline{R3c}$ nonpolar metallic to an R3c polar metallic phase through the loss of inversion symmetry (Figure 2.1a). Neutron diffraction, [1] 1Raman spectroscopy, [11] and optical spectroscopy [12] have shown that the A_{2u} soft phonon mode responsible for the transition involves a coordinated 0.5 Å displacement of Li atoms along the polar c-axis. [11] To explain these observations, several theories have been developed. [13–17] The decoupled electron mechanism hypothesis proposed by Puggioni et al. postulates that the soft phonon responsible for driving the "ferroelectric" transition is energetically decoupled from the electrons at the Fermi level responsible for the metallicity. In this picture, ineffective electron screening of long-range dipolar couplings stabilize the polar phase. [9,12,18] Benedek et al. proposed a related

mechanism that emphasizes short-range, atomic detail.[19] Here, ion-size mismatch effects and the local coordination preferences of the A-site Li atom are thought to drive the phase transition. With short-range interactions at the forefront, the itinerant electrons that are expected to screen the dipole−dipole forces are, thus, of secondary importance. In the high-temperature phase, the Li atom is coordinated to nine nearby O atoms via three short Li−O bonds and six long Li−O bonds. On the other hand, signatures of the polar metal phase include OsO_6 octahedral rotations that shorten three of the longer Li−O bonds, and Li atoms displacements that shorten the three short Li−O bonds. The overall effect of these structural changes is to octahedrally coordinate the Li atom in the polar metal phase[19] (Figure 2.1b). With regard to why all the Li atoms are displaced uniformly, their coordinated motion is thought to both minimize the number of faces Li octahedra share with Os octahedra and open up unscreened channels of anisotropic Coulomb interactions by which to minimize the free energy.[13,15] Hence, the Li-coordination environment plays a determining role in the stabilization of the polar metal phase, but an experimental viewpoint that takes both broken symmetries and core-level specificity into account is lacking. The most common probe of broken inversion symmetry is optical second harmonic generation (SHG) spectroscopy, which has been applied previously to examine the nature of Os−O bonding in $LiOsO_3$. [20] However, not only is optical SHG non-element-specific, but a partial density of states (DOS) analysis reveals overwhelming contributions of Os 5d and O 2p character around the Fermi level (Figure 2.1c and Section 6 in the Supporting Information (SI)).

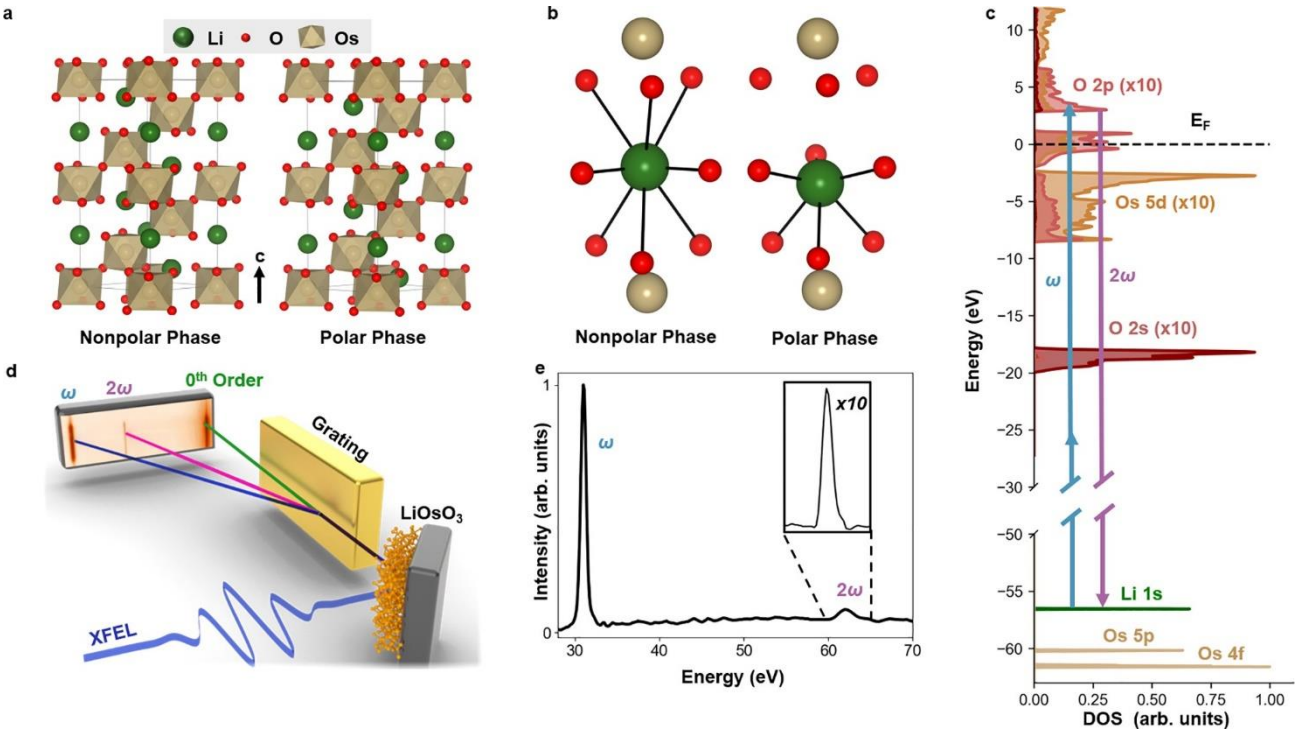

Figure 2.1. The structures of LiOsO3 in its nonpolar and polar phases, partial density of states calculations, and experimental scheme. (a) The hexagonal unit cell of LiOsO3 in its high-temperature nonpolar phase and low-temperature polar phase with the polar c-axis identified. (b) In the nonpolar phase, the Li atoms are symmetrically located between two OsO_6 octahedra from above and below and in plane with 3 nearby O atoms from adjacent OsO_6 octahedra. In the polar phase, an asymmetric displacement of Li atoms along the emergent polar c-axis results in octahedrally coordinated Li atoms. (c) Partial density of states calculations. Near the Fermi level are predominantly states of Os 2p and Os 5d character. The XUV-SHG experiment involves core-level electron excitations at 28−33 eV photon energy (ω) that are half-resonant with the Li 1s core state, resulting in second harmonic emission (2ω). Note the y-scale has broken axes between −50 eV and −30 eV. (d) Schematic of the experimental setup. The fundamental XUV beam is incident on the [120] plane of a LiOsO3 crystal under a 45° angle of incidence, with respect to the surface normal. The reflected beam is spectrally dispersed by a grating onto a detector, enabling simultaneous measurement of signals at the fundamental and SHG frequencies. (e) Acharacteristic spectrum measured at an incident XFEL energy of 31 eV, featuring peaks at both the fundamental and second harmonic. The inset shows the 2ω signal (×10) in detail, indicating excellent signal-to-noise.

In $LiOsO_3$, the features of interest are Li−O acentric displacements. Given that the orbital characters of states around the Fermi surface, it is not surprising then that an order-of-magnitude weaker optical SHG signal was found in $LiOsO_3$, compared to $LiTaO_3$ and $LiNbO_3$. [20]

To gain insight into the nature of the polar phase, we turn to extreme ultraviolet second harmonic generation (XUV-SHG) spectroscopy, which is a newly developed method viable for studying bulk-phase noncentrosymmetric masterials, [21] surfaces, [22,23] and buried interfaces[24] in the XUV or the soft X-ray (SXR) regimes, where the objective is to perform SHG under resonant conditions, and in the hard X-ray regime, where a nonresonant approach is usually taken. [25–27] In SXR- or XUV-SHG spectroscopy, the incident X-ray beam is resonant or half-resonant with a core-to-valence transition, such that the resulting resonantly enhanced, background-free signal is sensitive to core levels in the electronic structure. By energetically resolving the SHG emission, the symmetry breaking can be correlated to particular spectral features. The application of XUV-SHG spectroscopy to such short wavelengths, although it requires the use of XUV photon sources capable of achieving high pulse intensities to drive the nonlinear light-matter response, for which X-ray free electron lasers (XFEL) are uniquely well-suited. The inherent intensity fluctuations of XFEL sources measure on a shot-to-shot basis enable measuring the nonlinear response via

$$I(2\omega) \propto |\chi^{(2)}_{eff}(2\omega;\ \omega + \omega)|\, I(\omega)$$

where $\chi_{eff}^{(2)}$ is the effective nonlinear susceptibility, dependent on crystal cut and experimental geometry, the incident beam is at a frequency-dependent intensity, I(ω), and SHG emission occurs with a frequency of 2ω. Here, the dielectric environment around Li in $LiOsO_3$ below T_c is probed by tuning the incident XFEL photon energy to be half-resonant with energies around the Li K-edge at −56.6 eV (Figure 2.1c) with contributions from nearby Os semicore states. The energy-dependent $\chi_{eff}^{(2)}$ is extracted

according to eq 1 and ab initio density functional perturbation theory (DFPT) simulations are used to relate the nonlinear response to the broken inversion symmetry. We find that the resultant nonlinear susceptibility suggests sensitivity to Li atomic displacements in the unit cell, but a lack of OsO_6 octahedral rotations. Further, our results pave the way toward time- and temperature-dependent measurements of inversion symmetry-broken systems with core-level specificity.

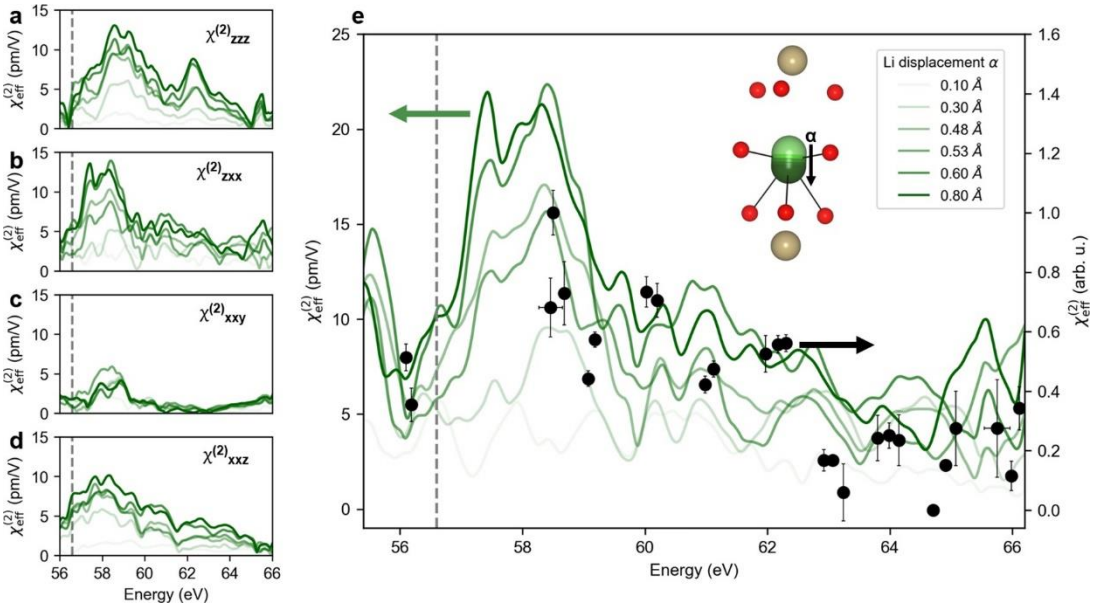

Figure 2.2: The energy-dependent nonlinear susceptibility across the Li K-edge. (a−d) $\chi_{zzz}^{(2)}$, $\chi_{zxx}^{(2)}$, $\chi_{xxy}^{(2)}$, and $\chi_{xxz}^{(2)}$ across the Li K-edge. (e) The experimentally determined nonlinear susceptibility shown black points overlaid onto the calculated $\chi_{eff}^{(2)}(2\omega)$. For panels (a-e), the dashed gray line at 56.6 eV corresponds to the onset of the Li K edge: darker green corresponds to larger Li displacement along the polar axis (α) of the $LiOsO_3$ polar phase as indicated by the inset in panel (e) and in the corresponding legend. Vertical error bars correspond to errors in the quadratic fit of eq1, whereas horizontal error bars are a result of energy jitter in the FEL.

2.2. Experimental Results

XUV-SHG spectroscopy was performed on samples of $LiOsO_3$ in its polar metal phase at T = 62 K and T = 160 K at the BL1 beamline of the SPring-8 Å Compact Free Electron Laser (SACLA).[28] A 30 fs p-polarized XUV beam was incident at 45°, with respect to the surface normal onto the [120] plane of $LiOsO_3$. By tuning the incident

photon energy to energies ranging from 28 eV to 33 eV, the incident photon was half-resonant with the Li 1s (−56.6 eV) level and close-by Os 4f (−61.6 eV) and 5p (−60.2 eV) levels, thus requiring two incident photons to access the valence states (Figure 2.1c). XUV-SHG spectra were collected by energy-dispersing the outgoing beam with a grating to simultaneously observe the fundamental and second harmonic beams using an imaging spectrometer (Figures 2.1d-e). Through nonlinear effects, a p-polarized fundamental photon can result in a nontrivial weighting of both s- and p-polarized frequency-doubled photons. An estimation of the relative contribution of both channels is provided in Section S1 in the SI, but further polarization analysis is beyond the scope of this work, since the two polarizations are not experimentally resolved. The $\chi_{eff}^{(2)}$ spectrum was then extracted using eq 1 after binning and averaging spectra based on the photon energy and intensity of the driving fundamental pulse. The inherent jitter of the XFEL, both in frequency and intensity, allowed for a high-fidelity extraction of $\chi_{eff}^{(2)}(2\omega)$ with significantly more data points, compared to refs 21−24. For the T = 62 K set of measurements, a quadratic function was fit to a plot of I(ω) vs I(2ω), at each energy where the second-order fit coefficient is modulo $|\chi_{eff}^{(2)}(2\omega)|^2$, with $\chi_{eff}^{(2)}(2\omega)$ a rank-three tensor of four independent components ($\chi_{zzz}^{(2)}$,$\chi_{xxz}^{(2)}$, $\chi_{zxx}^{(2)}$, and $\chi_{xxy}^{(2)}$), because of point group symmetry (Figure 2.2e). For the measurements at 160 K, no SHG signal was discernible above the background noise, in accordance with the centrosymmetry of the $LiOsO_3$ high-temperature phase. The lack of observable SHG above Tc further serves to rule out that the SHG from the low-temperature phase comes from broken inversion symmetry at the surface or harmonic contamination in the FEL beam.

In order to relate the measured nonlinear susceptibility to unit cell structure, a tensor analysis considering the experiment geometry and crystal cut was performed to arrive at a mathematical expression for $\chi_{eff}^{(2)}$. Further details of the experimental setup, data analysis, and sample preparation are described in sections S0−S4 in the SI.

According to selection rules for SHG, electrons residing in Li 1s core states can transition to valence states of Os 5d character, whereas the Os 5p and Os 4f semicore states can transition to valence states of O 2p character (Figure 2.1c). The approximately 2 eV-wide gap in the DOS above the Fermi level (E_F) has been previously assigned to the crystal-field splitting in Os 5d-like orbitals, but the nonzero DOS directly at E_F is consistent with the metallic character of LiOsO3.[16]

To gain insight how the measured spectra relate to the Li coordination environment, theoretical calculations of the $LiOsO_3$ linear absorption were performed using the exciting full-potential all-electron-augmented linearized planewave software package based on first-principles density function theory (DFT).[29] Two $LiOsO_3$ periodic cell structures, corresponding to the nonpolar and polar phases, were used. The Brillouin zone was sampled with a 15 × 15 × 15 Γ-point centered k-point grid with the local density approximation functional.[30] DFPT simulations within the random phase approximation were used to access excited states of the system. The formalism outlined by Sharma et al., as implemented within exciting, was used calculate the four active $\chi_{ijk}^{(2)}$ tensor elements (see Figures 2.2a−d), with the aforementioned k-point grid set.[31] 120 empty states were included in the ground-state calculation to account for the excited state at double the energy of the Li 1s core state. The background signal, which is the

response from the valence electrons and is proportional to the inverse of energy (~1/energy), was subtracted to obtain the effective susceptibility from the core state. The $\chi_{eff}^{(2)}$ was next calculated as a function of varying Li position along the polar axis, α, and compared to the experimental results (Figure 2.2e). Simulations with OsO_6 displacements were also performed (see Section S7 in the SI) showing only little effect on the resulting XUV-SHG spectra. In addition, the core-level nonlinear susceptibility (see Section S8 in the SI), was calculated with the exclusion of Li 1s states (see Section S9 in the SI), the results of which suggest that the nonlinear response within the energy range probed is predominantly due to transition from Li 1s core states to states above the Fermi level. Finally, the DFT calculations were repeated using the Vienna ab initio software package (VASP[32]), using a projector augmented wave (PAW) approach and a plane wave basis set of up to 400 eV to visualize the Kohn−Sham equation-generated charge densities within the $LiOsO_3$ unit cell. Shown in Figure 2.3 are projections of this charge density surface onto the [110] plane through the middle of the hexagonal unit cell.

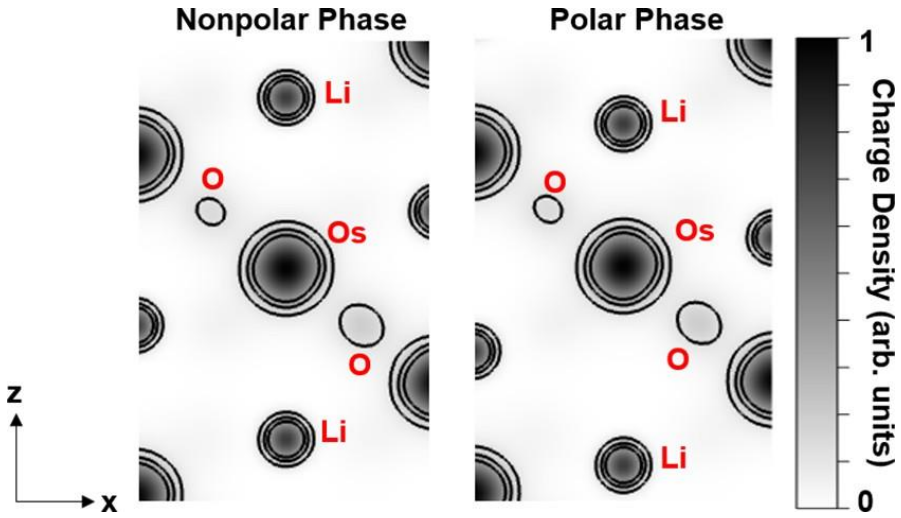

Figure 2.3. Charge densities within the LiOsO3 unit cell. Charge densities along the polar axis reveal inversion symmetry is broken in the polar phase as Li atoms are displaced vertically along the polar z axis. An applied electric field along the z-axis further increases the magnitude of this asymmetry, whereas an applied electric field in the xy-plane increases it nontrivially. The black contours are drawn at 0.15 intervals of charge density units, from 0 to 0.6 arb.

2.3. Discussion

Absolute values of $\chi_{eff}^{(2)}$ in the XUV are predicted are calculated to be on the order of 10 pm/V, which is in accordance with measured nonlinear susceptibilities of LiOsO3 and chemically similar $LiTaO_3$ and $LiNbO_3$ in the optical regime.[20,33] The experimentally determined $\chi_{eff}^{(2)}$ shown in Figure 2.2e has several features to point out. DFT calculations in which the Li 1s states are removed from the simulation basis set indicate that the XUV-SHG signal in the 56−59 eV range is a result of transitions from Li 1s states (see Figure 2S7.1 in the SI). This is supported by the observation in Figure 2.2e that the spectral feature centered at 58 eV is highly sensitive to Li atom position within the unit cell. The increase in SHG signal measured experimentally suggests that XUV-SHG is sensitive to Li atomic displacements with core-level specificity. Furthermore, DFT simulations involving OsO_6 octahedral rotations indicate that such motions have a very minimal affect the core-level $\chi_{eff}^{(2)}$ spectrum (Figure 2.S8.1 and 2.S9.1). This

observation, combined with the decreasing SHG response in the energy range above 60 eV corresponding to electronic transitions from Os semicore to O 2p states, suggesting that inversion symmetry is largely maintained around the Os atoms. Next, we turn to an analysis of how the XUV-SHG spectrum varies as a function of Li displacement α. The main feature at 58 eV increases in magnitude with asymmetry in the Li−O dipoles along the polar axis, resulting from one of two factors: (a) the mere increase in the asymmetric distortion enhances the XUV-SHG signal, or (b) as Li ions are displaced toward OsO_6 octahedra, the aforementioned Li−O "long bonds" get shorter, leading to increased hybridization between orbitals of Li 2s and Os 2p character. This, in turn, gives more s-character to O 2p orbitals, thus opening up more selection-rule-allowed states for Li 1s electrons to transition into. The latter possibility is supported by DFT simulations since increased hybridization should lead to a downward shift in energy and a change in the density of states, which is observed in the appearance of a changing peak shape and a spectral shoulder at 57.5 eV as α increases. To gain further insight into the inversion symmetry-breaking process, projections of the calculated charge density surface onto the [110] plane of the real space unit cell were examined. Shown in Figure 2.3 are slices of the charge density surfaces cut along the [110] plane in both the polar and nonpolar phases of $LiOsO_3$. It is immediately apparent that the polar phase is characterized by broken inversion symmetry around the Li ions, as evidenced by the unequal relative displacements of each of the Li atoms to the central Os atom in the polar phase. The plots in Figure 2.3 provide further qualitative physical intuition behind spectral features of the tensor elements shown in Figures 2.2a−d. Here, it should be noted that the i^{th} index in $\chi_{ijk}^{(2)}$ corresponds to the Cartesian direction along which dipole oscillations are

generated at with a frequency of 2ω by driving electric fields along the j^{th} and k^{th} directions. The broad feature at 58 eV observed in the calculated spectra for $\chi_{zzz}^{(2)}$ and $\chi_{zxx}^{(2)}$ can be attributed to the polar displacement of Li atoms along the z-axis as the primary contributor to the broken inversion symmetry in $LiOsO_3$. It can also be seen that $\chi_{zzz}^{(2)}$ and $\chi_{xxz}^{(2)}$ increase in magnitude, but with a relatively unchanged spectral shape as α increases. In contrast, $\chi_{zxx}^{(2)}$ exhibits a nontrivial α-dependence. These observations can be contextualized by comparing the nonpolar and polar charge densities in Figure Here, it is apparent that driving with a fundamental pulse along the z-direction will increase the asymmetry along the polar axis. Increasing α merely increases the amplitude of these oscillations. On the other hand, an incident laser beam polarized along the x-direction will alter the electron density with respect to the already present Li displacement in a complex way. Lastly, it is of note that $\chi_{xxy}^{(2)}$ changes minimally with α. This can again by explained by the observation that there are minimal polar displacements within the x−y plane for all atomic environments within the unit cell. In summary, it is shown that XUV-SHG can selectively probe inversion-breaking symmetry in a bulk material with core-level specificity. Compared to optical SHG methods, XUV-SHG spectroscopy fills a key gap for studying structural asymmetries when the structural distortion is energetically separated from the Fermi surface and for probing symmetry-breaking in the spectral features of interest. For example, optical SHG would primarily probe Os−O acentric displacements, which obscures the Li−O acentric displacements that are the physics of interest. In addition, XUV-SHG offers the ability to access information on light atoms in a heavy-atom environment by making use of core-level resonances. A comparison of calculated charge density plots and theoretical

simulations of the how the nonlinear susceptibility tensor elements vary as a function of Li displacement provide a qualitative picture for how microscopic asymmetries on unit cell length scales determine the nonlinear response. Open questions for future investigation are highlighted in three recent works. Shan et al.[34] observed SHG due to electric quadrupolar effects above the polar ordering temperature up to 230 K, as a result of an extended critical fluctuation region. Such effects were not visible in XUV-SHG at 160 K, but may have been below the detection limit of this experiment. Through complementary theory calculations, Helk et al.[23] noted that resonant and nonresonant contributions to SHG can be of the same order of magnitude in the XUV regime, because of allowed transitions from the valence band to high-energy continuum states. Further development of SHG methodology in the XUV and SXR regimes will be essential to deconvolute these contributions and to fully characterize element-specific responses. Lastly, we have recently demonstrated polarization-resolved XUV-SHG[35] as a viable method to extract symmetry information from angle-resolved SHG responses with core-level specificity. Such a tool will add invaluable insight into systems like $LiOsO_3$ where symmetry-arguments and angular anisotropies are central to structure−function relationships. We point out that the future of XUV-SHG spectroscopy lies in its potential to track the nonlinear response as a function of both temperature and time. The sensitivity to Li atom displacement above and below T_c demonstrated here highlight the viability for XUV-SHG for studying critical fluctuations, phase transitions, and interface physics in other condensed matter systems.

2.4. Acknowledgements

Chapter 2, in full, is a reprint of the material as it appears in *Nano Letters* **2021** *21* (14), 6095-6101. Emma Berger, Sasawat Jamnuch, Can B. Uzundal, Clarisse Woodahl, Hari Padmanabhan, Angelique Amado, Paul Manset, Yasuyuki Hirata, Yuya Kubota, Shigeki Owada, Kensuke Tono, Makina Yabashi, Cuixiang Wang, Youguo Shi, Venkatraman Gopalan, Craig P. Schwartz, Walter S. Drisdell, Iwao Matsuda, John W. Freeland, Tod A. Pascal, and Michael Zuerch. The dissertation author was the primary investigator of the theoretical part and author of this paper. Emma Berger and Sasawat Jamnuch have equal contributions to the work.

2.5. Chapter 2 References

(1) Shi, Y.; Guo, Y.; Wang, X.; Princep, A. J.; Khalyavin, D.; Manuel, P.; Michiue, Y.; Sato, A.; Tsuda, K.; Yu, S.; Arai, M.; Shirako, Y.; Akaogi, M.; Wang, N.; Yamaura, K.; Boothroyd, A. T. A Ferroelectric-like Structural Transition in a Metal. Nat. Mater. 2013, 12 (11), 1024−1027.

(2) Anderson, P. W.; Blount, E. I. Symmetry Considerations on Martensitic Transformations: "Ferroelectric" Metals? (Physical Review Letters). Phys. Rev. Lett. 1965, 14 (7), 217−219.

(3) Puggioni, D.; Giovannetti, G.; Capone, M.; Rondinelli, J. M. Design of a Mott Multiferroic from a Nonmagnetic Polar Metal. Phys. Rev. Lett. 2015, 115 (8), 087202.

(4) Puggioni, D.; Giovannetti, G.; Rondinelli, J. M. Polar Metals as Electrodes to Suppress the Critical-Thickness Limit in Ferroelectric Nanocapacitors. J. Appl. Phys. 2018, 124 (17), 174102.

(5) Edelstein, V. M. Features of Light Reflection off Metals with Destroyed Mirror Symmetry. Phys. Rev. B: Condens. Matter Mater. Phys. 2011, 83 (11), 113109.

(6) Edelstein, V. M. Magnetoelectric Effect in Polar Super-conductors. Phys. Rev. Lett. 1995, 75 (10), 2004−2007.

(7) Edelstein, V. M. Magnetoelectric Effect in Dirty Super-conductors with Broken Mirror Symmetry. Phys. Rev. B: Condens. Matter Mater. Phys. 2005, 72 (17), 172501.

(8) Enderlein, C.; de Oliveira, J. F.; Tompsett, D. A.; Saitovitch, E. B.; Saxena, S. S.; Lonzarich, G. G.; Rowley, S. E. Superconductivity Mediated by Polar Modes in Ferroelectric Metals. Nat. Commun. 2020, 11 (4852), 1−10.

(9) Puggioni, D.; Rondinelli, J. M. Designing a Robustly Metallic Noncenstrosymmetric Ruthenate Oxide with Large Thermopower Anisotropy. Nat. Commun. 2014, 5 (3432), 1−9.

(10) Fei, Z.; Zhao, W.; Palomaki, T. A.; Sun, B.; Miller, M. K.; Zhao, Z.; Yan, J.; Xu, X.; Cobden, D. H. Ferroelectric Switching of a Two-Dimensional Metal. Nature 2018, 560 (7718), 336−339.

(11) Jin, F.; Wang, L.; Zhang, A.; Ji, J.; Shi, Y.; Wang, X.; Yu, R.; Zhang, J.; Plummer, E. W.; Zhang, Q. Raman Interrogation of the Ferroelectric Phase Transition in Polar Metal $LiOsO_3$. Proc. Natl. Acad. Sci. U. S. A. 2019, 116 (41), 20322−20327.

(12) Laurita, N. J.; Ron, A.; Shan, J. Y.; Puggioni, D.; Koocher, N. Z.; Yamaura, K.; Shi, Y.; Rondinelli, J. M.; Hsieh, D. Evidence for the Weakly Coupled Electron Mechanism in an Anderson-Blount Polar Metal. Nat. Commun. 2019, 10 (3217), 1−7.

(13) Xiang, H. J. Origin of Polar Distortion in $LiNbO_3$ -Type “Ferroelectric” Metals: Role of A -Site Instability and Short-Range Interactions. Phys. Rev. B: Condens. Matter Mater. Phys. 2014, 90 (9), 094108.

(14) Jin, F.; Zhang, A.; Ji, J.; Liu, K.; Wang, L.; Shi, Y.; Tian, Y.; Ma, X.; Zhang, Q. Raman Phonons in the Ferroelectric-like Metal $LiOsO_3$. Phys. Rev. B: Condens. Matter Mater. Phys. 2016, 93 (6), 064303.

(15) Liu, H. M.; Du, Y. P.; Xie, Y. L.; Liu, J. M.; Duan, C. G.; Wan, X. Metallic Ferroelectricity Induced by Anisotropic Unscreened Coulomb Interaction in $LiOsO_3$. Phys. Rev. B: Condens. Matter Mater. Phys. 2015, 91 (6), 064104.

(16) Lo Vecchio, I.; Giovannetti, G.; Autore, M.; Di Pietro, P.; Perucchi, A.; He, J.; Yamaura, K.; Capone, M.; Lupi, S. Electronic Correlations in the Ferroelectric Metallic State of $LiOsO_3$. Phys. Rev. B: Condens. Matter Mater. Phys. 2016, 93 (16), 1−5.

(17) Sim, H.; Kim, B. G. First-Principles Study of Octahedral Tilting and Ferroelectric-like Transition in Metallic $LiOsO_3$. Phys. Rev. B: Condens. Matter Mater. Phys. 2014, 89, 201107.

(18) Kim, T. H.; Puggioni, D.; Yuan, Y.; Xie, L.; Zhou, H.; Campbell, N.; Ryan, P. J.; Choi, Y.; Kim, J. W.; Patzner, J. R.; Ryu, S.; Podkaminer, J. P.; Irwin, J.; Ma, Y.; Fennie, C. J.; Rzchowski, M. S.; Pan, X. Q.; Gopalan, V.; Rondinelli, J. M.; Eom, C. B. Polar Metals by Geometric Design. Nature 2016, 533 (7601), 68−72.

(19) Benedek, N. A.; Birol, T. Ferroelectric" Metals Reexamined: Fundamental Mechanisms and Design Considerations for New Materials. J. Mater. Chem. C 2016, 4, 4000−4015.

(20) Padmanabhan, H.; Park, Y.; Puggioni, D.; Yuan, Y.; Cao, Y.; Gasparov, L.; Shi, Y.; Chakhalian, J.; Rondinelli, J. M.; Gopalan, V. Linear and Nonlinear Optical Probe of the Ferroelectric-like Phase Transition in a Polar Metal, $LiOsO_3$. Appl. Phys. Lett. 2018, 113, 122906.

(21) Yamamoto, S.; Omi, T.; Akai, H.; Kubota, Y.; Takahashi, Y.; Suzuki, Y.; Hirata, Y.; Yamamoto, K.; Yukawa, R.; Horiba, K.; Yumoto, H.; Koyama, T.; Ohashi, H.; Owada, S.; Tono, K.; Yabashi, M.; Shigemasa, E.; Yamamoto, S.; Kotsugi, M.; Wadati, H.; Kumigashira, H.; Arima, T.; Shin, S.; Matsuda, I. Element Selectivity in Second-Harmonic Generation of $GaFeO_3$ by a Soft-X-Ray Free-Electron Laser. Phys. Rev. Lett. 2018, 120, 223902.

(22) Lam, R. K.; Raj, S. L.; Pascal, T. A.; Pemmaraju, C. D.; Foglia, L.; Simoncig, A.; Fabris, N.; Miotti, P.; Hull, C. J.; Rizzuto, A. M.; Smith, J. W.; Mincigrucci, R.; Masciovecchio, C.; Gessini, A.; Allaria, E.; De Ninno, G.; Diviacco, B.; Roussel, E.; Spampinati, S.; Penco, G.; Di Mitri, S.; Trovò, M.; Danailov, M.; Christensen, S. T.; Sokaras, D.; Weng, T. C.; Coreno, M.; Poletto, L.; Drisdell, W. S.; Prendergast, D.; Giannessi, L.; Principi, E.; Nordlund, D.; Saykally, R. J.; Schwartz, C. P. Soft X-Ray Second Harmonic Generation as an Interfacial Probe. Phys. Rev. Lett. 2018, 120, 023901.

(23) Helk, T.; Berger, E.; Jamnuch, S.; Hoffmann, L.; Kabacinski, A.; Gautier, J.; Tissandier, F.; Goddet, J.-P.; Chang, H.-T.; Oh, J.; Pemmaraju, C. Das; Pascal, T. A.; Sebban, S.; Spielmann, C.; Zuerch, M. Table-Top Extreme Ultraviolet Second Harmonic Generation. Sci. Adv. 2021, 7, eabe2265.

(24) Schwartz, C. P.; Raj, S. L.; Jamnuch, S.; Hull, C. J.; Miotti, P.; Lam, K.; Nordlund, D.; Uzundal, C. B.; Pemmaraju, C. Das Ångström-Resolved Interfacial Structure in Organic−Inorganic Junctions. Arxiv 2020, 2005.01905, 1−19, accessed June 1, 2021.

(25) Shwartz, S.; Fuchs, M.; Hastings, J. B.; Inubushi, Y.; Ishikawa, T.; Katayama, T.; Reis, D. A.; Sato, T.; Tono, K.; Yabashi, M.; Yudovich, S.; Harris, S. E. X-Ray Second Harmonic Generation. Phys. Rev. Lett. 2014, 112, 163901.

(26) Fuchs, M.; Trigo, M.; Chen, J.; Ghimire, S.; Shwartz, S.; Kozina, M.; Jiang, M.; Henighan, T.; Bray, C.; Ndabashimiye, G.; Bucksbaum, P. H.; Feng, Y.; Herrmann, S.; Carini, G. A.; Pines, J.; Hart, P.; Kenney, C.; Guillet, S.; Boutet, S.; Williams, G. J.; Messerschmidt, M.; Seibert, M. M.; Moeller, S.; Hastings, J. B.; Reis, D. A. Anomalous Nonlinear X-Ray Compton Scattering. Nat. Phys. 2015, 11, 964−970.

(27) Yudovich, S.; Shwartz, S. Second-Harmonic Generation of Focused Ultrashort x-Ray Pulses. J. Opt. Soc. Am. B 2015, 32 (9), 1894−1900.

(28) Owada, S.; Togawa, K.; Inagaki, T.; Hara, T.; Tanaka, T.; Joti, Y.; Koyama, T.; Nakajima, K.; Ohashi, H.; Senba, Y.; Togashi, T.; Tono, K.; Yamaga, M.; Yumoto, H.; Yabashi, M.; Tanaka, H.; Ishikawa, T. A Soft X-Ray Free-Electron Laser Beamline at SACLA: The Light Source, Photon Beamline and Experimental Station. J. Synchrotron Radiat. 2018, 25, 282−288.

29) Gulans, A.; Kontur, S.; Meisenbichler, C.; Nabok, D.; Pavone, P.; Rigamonti, S.; Sagmeister, S.; Werner, U.; Draxl, C. Exciting: A Full-Potential All-Electron Package Implementing Density-Functional Theory and Many-Body Perturbation Theory. J. Phys.: Condens. Matter 2014, 26, 363202.

(30) Perdew, J. P.; Zunger, A. Self-Interaction Correction to Density-Functional Approximations for Many-Electron Systems. Phys. Rev. B: Condens. Matter Mater. Phys. 1981, 23 (10), 5048−5079.

(31) Sharma, S.; Ambrosch-Draxl, C. Second-Harmonic Optical Response from First Principles. Phys. Scr. 2004, T109, 128−134.

(32) Kresse, G.; Furthmüller, J. Efficient Iterative Schemes for Ab Initio Total-Energy Calculations Using a Plane-Wave Basis Set. Phys. Rev. B: Condens. Matter Mater. Phys. 1996, 54 (16), 11169−11186.

(33) Schiek, R.; Pertsch, T. Absolute Measurement of the Quadratic Nonlinear Susceptibility of Lithium Niobate in Waveguides. Opt. Mater. Express 2012, 2 (2), 126−139.

(34) Shan, J.-Y.; de la Torre, A.; Laurita, N. J.; Zhao, L.; Dashwood, C. D.; Puggioni, D.; Wang, C. X.; Yamaura, K.; Shi, Y.; Rondinelli, J. M.; Hsieh, D. Evidence for an Extended Critical Fluctuation Region above the Polar Ordering Transition in $LiOsO_3$. Phys. Rev. Res. 2020, 2, 033174.

(35) Uzundal, C. B.; Jamnuch, S.; Berger, E.; Woodahl, C.; Manset, P.; Hirata, Y.; Sumi, T.; Amado, A.; Akai, H.; Kubota, Y.; Owada, S.; Tono, K.; Yabashi, M.; Freeland, J. W.; Schwartz, C. P.; Drisdell, W. S.; Matsuda, I.; Pascal, T. A.; Zong, A.; Zuerch, M. Polarization- Resolved Extreme Ultraviolet Second Harmonic Generation from $LiNbO_3$. Arxiv 2021, No. 2104.01313, accessed June 1, 2021.

CHAPTER 3

ANGSTROM-RESOLVED INTERFACIAL STRUCTURE IN BURIED ORGANIC-INORGANIC JUNCTIONS

3.1. **Abstract**

Charge transport processes at interfaces play a crucial role in many processes. Here, the first soft x-ray second harmonic generation (SXR SHG) interfacial spectrum of a buried interface (boron–Parylene N) is reported. SXR SHG shows distinct spectral features that are not observed in x-ray absorption spectra, demonstrating its extraordinary interfacial sensitivity. Comparison to electronic structure calculations indicates a boron-organic separation distance of 1.9 Å, with changes of less than 1 Å resulting in easily detectable SXR SHG spectral shifts (ca. hundreds of milli-electron volts).

3.2. **Introduction**

Surfaces and interfaces play central roles in a variety of critical biological systems, electronics, batteries, and catalytic systems. Key chemical reactions and physical processes depend explicitly on the electronic structure of the interface and the dynamics across it. Experimentally, surfaces are often studied using a range of spectroscopic and imaging techniques, from grazing incidence x-ray scattering[1,2], to scanning probe[3,4] and total internal reflection[5–7] spectroscopies. These methods, however, are unsuited for the study of buried functional interfaces, which often govern critical chemical and physical processes. Interfaces between two bulk materials, or surfaces coated with macroscopically thick (hundreds of nanometers or greater) capping layers, cannot be

specifically probed using these techniques. Absorption of photons by the bulk materials prevents optical probes from even reaching such interfaces, and the photoelectrons generated at the buried interface by high penetration x-ray probes cannot escape. Visible and IR second harmonic generation (SHG) and sum frequency generation (SFG) [8, 9] do not suffer from these limitations of studying buried interfaces. These techniques have been used for a variety of applications including characterization of semiconductors, solar cell devices, and biological structures[10–12]. While these techniques are quite powerful, they typically provide information about vibrational dynamics or valence transitions, and lack the elemental specificity of x-ray techniques. Until recently, x-ray nonlinear spectroscopy was precluded by the lack of available light sources with sufficient coherence and flux, but the recent advent of x-ray free electron lasers (FELs) that generate femtosecond pulses with high peak powers and coherence has enabled such experiments [13–15]. Soft x-ray SHG (SXR SHG) offers powerful advantages compared to other surface-specific techniques[16, 17]. It has high penetration depth and combines the element specificity of x-ray absorption spectroscopy with the interfacial specificity of second order nonlinear spectroscopies. Linear x-ray absorption spectroscopy (XAS) is a generally useful tool for studying compounds as it is element specific and sensitive to the chemical and molecular environment of a target atom. Element-specific measurements of core-to-valence transitions can resolve individual contributions to the electronic structure, which is not easily possible in optical spectroscopies that detect valence-to-valence or vibrational transitions. This is especially important for disentangling the contributions from hybridization at interfaces. While x rays are highly penetrating, the use of different detection methods provides a range of depth

sensitivities: transmission measurements are bulk sensitive, fluorescence detection is sensitive to approximately 1 μm thick slabs based on the penetration of the photons[18], and photoelectron or total electron yield (TEY) detection provides sensitivity of a few nanometers due to the limited escape depth of photoelectrons[19–23]. Exploiting soft x-ray SHG has the potential for even higher surface sensitivity, since second harmonic (SH) photons are generated only from regions with broken centrosymmetry. Note that for hard x-ray radiation (>5 keV; <0.25 nm), the wavelength is short enough that the electric field is sensitive to inhomogeneities on an atomic scale, and the SH is generated throughout the material, rendering it bulk sensitive[24,25]. Instead, soft x-ray SH is generated only from 1–3 atomic layers at surfaces and interfaces of centrosymmetric media, as shown recently in the first demonstration of SXR SHG[16]. SXR SHG provides detailed electronic structure information analogous to that probed by x-ray absorption, with specificity for interfaces and no requirement for smooth surfaces. The element specificity of SXR SHG also reduces extraneous signals from interfaces containing other elements in a multilayer system. It is therefore ideally suited for the study of buried interfaces, but experimental proof is thus far lacking.

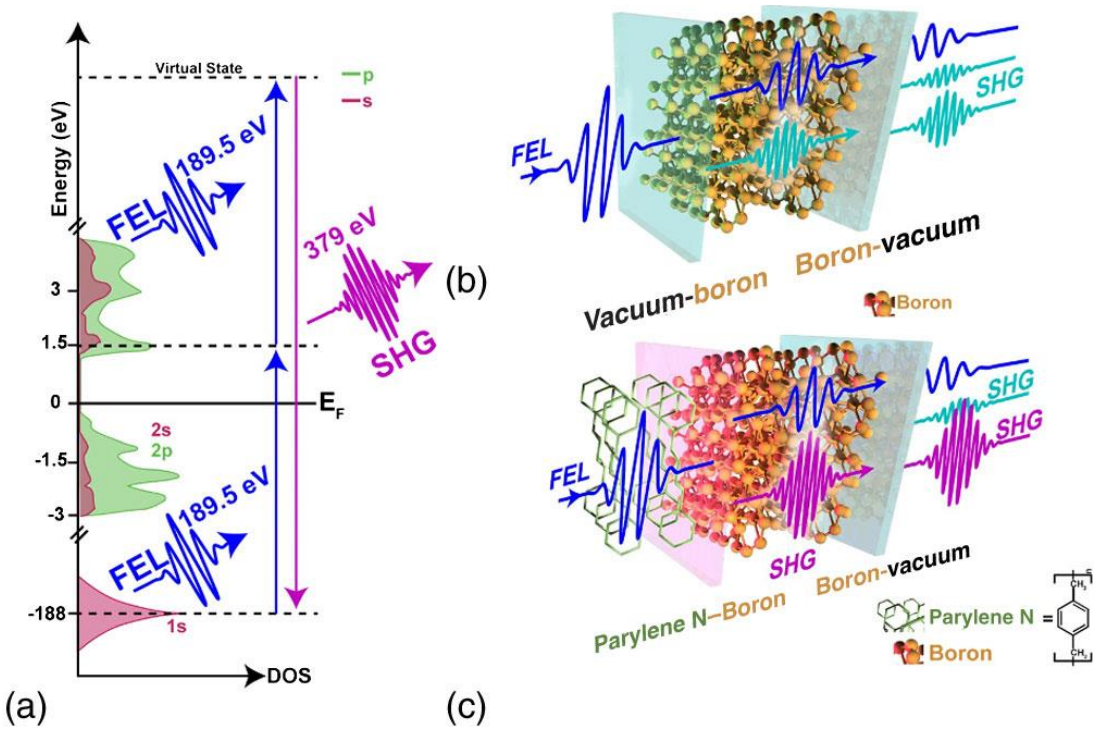

Figure. 3.1. Schematic of SHG from interfaces. In the energy level diagram (a), the density of states of boron (s-type red, p-type green) is resonantly pumped with an FEL pulse (blue). Because of selection rules, only the p-type states are probed. Two photons at this energy combine in the material and a second harmonic photon at twice the energy (purple) is emitted. The input energy is shown at 189.5 eV, generating a photon of 379 eV. During the experiment, the FEL energy was scanned from 184–196 eV. Two different interfaces were studied here, the (b) boron-vacuum interface and a (c) Parylene N–boron interface. The back boron-vacuum interface also generates some SHG signal (shown in light blue), but it will be less intense due to attenuation of the FEL pulse from transmission through the sample.

3.3. **Experimental Result and Discussion**

Here, we demonstrate the application of SXR SHG for probing the buried interface of a boron film with a support layer of Parylene N, a prototypical organic-inorganic interface. In the experiment, we compare the SXR SHG spectra of the boron-vacuum (B-V) and boron–Parylene N (B-PN) interfaces (Fig. 3.1), providing the first demonstration of probing the element-resolved electronic structure at a buried interface. To compare the interfacial sensitivity of SXR SHG to that of TEY XAS, we measured TEY XAS of

similar samples (see Supplemental Material for details[26]) using drain current for electron detection. The TEY XAS spectra of the B-V and B-PN samples are largely indistinguishable, because the probe depth of <10 nm is too large. By contrast, the SXR SHG measurements show clear differences between B-V and B-PN interfaces, allowing a detailed determination of the bond characteristics. Accompanying detailed first principles' calculations of SXR SHG spectra for both interfaces permits a detailed interpretation, showing that the observed experimental shift between the two spectra is due to boron interactions with Parylene N, indicating a strong surface spectral sensitivity to weak interactions, like London dispersion forces.

At the EIS-TIMEX beamline at the free-electron laser (FEL) FERMI[43], the SHG signal from the sample was detected using the same apparatus as in our recently reported study [16]. Nine different soft x-ray photon energies in the range from 184 to 200 eV were used. These fundamental input energies were just below, at, and just above the boron K edge[44]. The input intensity (I_0) of the FEL was determined from the drain current of an ellipsoidal mirror upstream of the sample. The samples comprised an unsupported 200 nm boron film and a 200 nm boron film with a 100 nm Parylene N support layer, purchased from Lebow Corporation. TEY x-ray absorption spectra of the two materials were collected at Beamline 8-2 at SSRL with the Parylene N layer 10 nm to enhance signal and the sample was mounted on silicon[45, 46]. In our previous x-ray SHG study, it was found that the SHG signals were very sensitive to the quality of the FEL laser pulse [16]. Therefore, each FEL shot was filtered by the energy spectrum of the pulse collected before the sample[47]. The intensity of the generated SHG response is given by the relation

$$I_{SHG} \propto |\chi^{(2)}|^2 I(\omega)^2$$

where $|\chi^{(2)}|$ is the second order nonlinear susceptibility of the interfacial layer of boron atoms. The SXR SHG intensity was plotted proportionally to I_0^2 (assuming constant pulse length and spot size) for each input energy and fit with a linear regression. As can be seen in the equation, the resulting slope is proportional to $|\chi^{(2)}|^2$. Finally, this slope was plotted as a function of photon energy to generate the nonlinear spectrum of the material properties at the surface or interface.

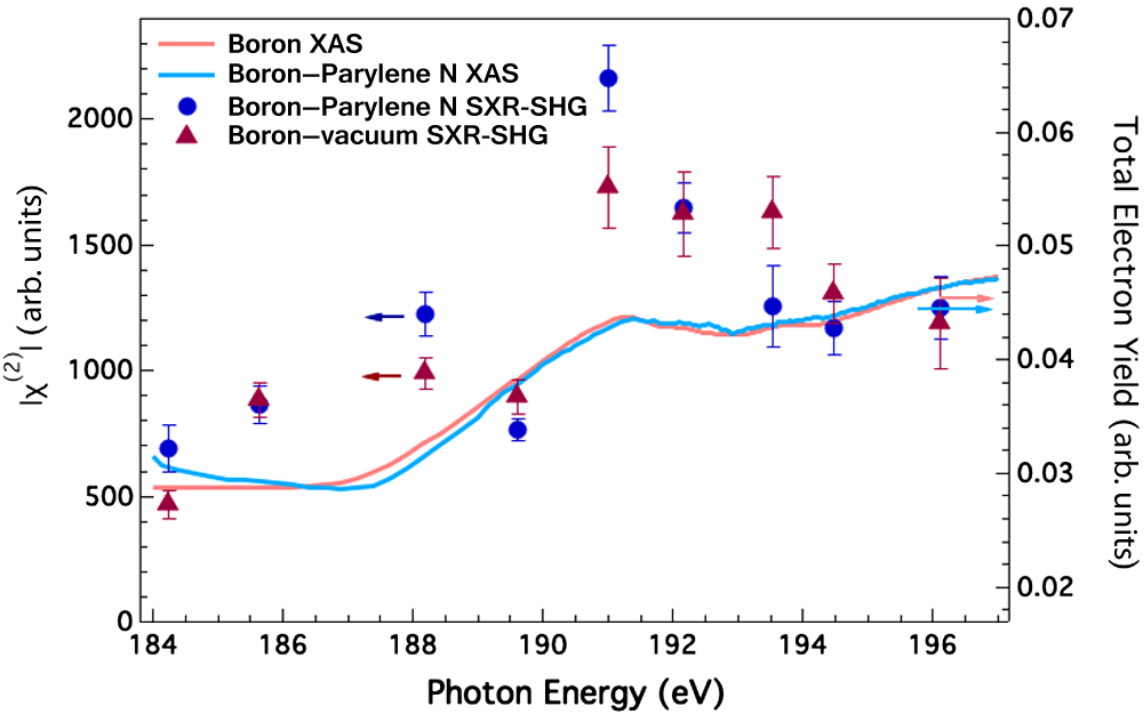

Figure. 3.2. Second harmonic generation spectra of the boron-vacuum and boron–Parylene N interfaces. The SHG spectrum of the B-V (dark red triangle) and B-PN (dark blue circle) interfaces, shown along with the linear x-ray absorption of the boron film (light red) and boron Parylene N multilayer film (light blue). The differences in the x-ray absorption spectra are believed to be due to the differences in the background and attempts to correct for it. $|\chi^{(2)}|^2$, determined from the linear regression slope of the SHG signal vs I_0^2. $|\chi^{(2)}|^2$, is significantly higher at the boron K edge for B-PN than for B-V. The error in FEL energy is smaller than the width of the marker size.

The measured SXR SHG spectra of the B-V and B-PN interfaces are shown in Fig. 3.2. Resonance effects can be seen in both spectra, as the SXR SHG intensity increases when

the fundamental energy is at or above the boron K edge. There is an increase in cross section of B-PN compared to B-V at 188 eV, 191 eV, and a decrease at 193.5 eV. Most notably, we observe a substantial increase in the nonlinear response at energies slightly above the B K-absorption edge. We attribute this to dipole-allowed resonant transitions from 1s to unoccupied states with B p character. The nonlinear response of this spectral region therefore becomes highly sensitive to the electronic valence structure of the interfacial bonds. The second photon absorption process, into a virtual state well above the conduction band to complete the SHG process, is non-resonant and thus less sensitive to the interfacial bonds. Well below and well above the edge, the SXR SHG spectra of B-V and B-PN are within error of each other.

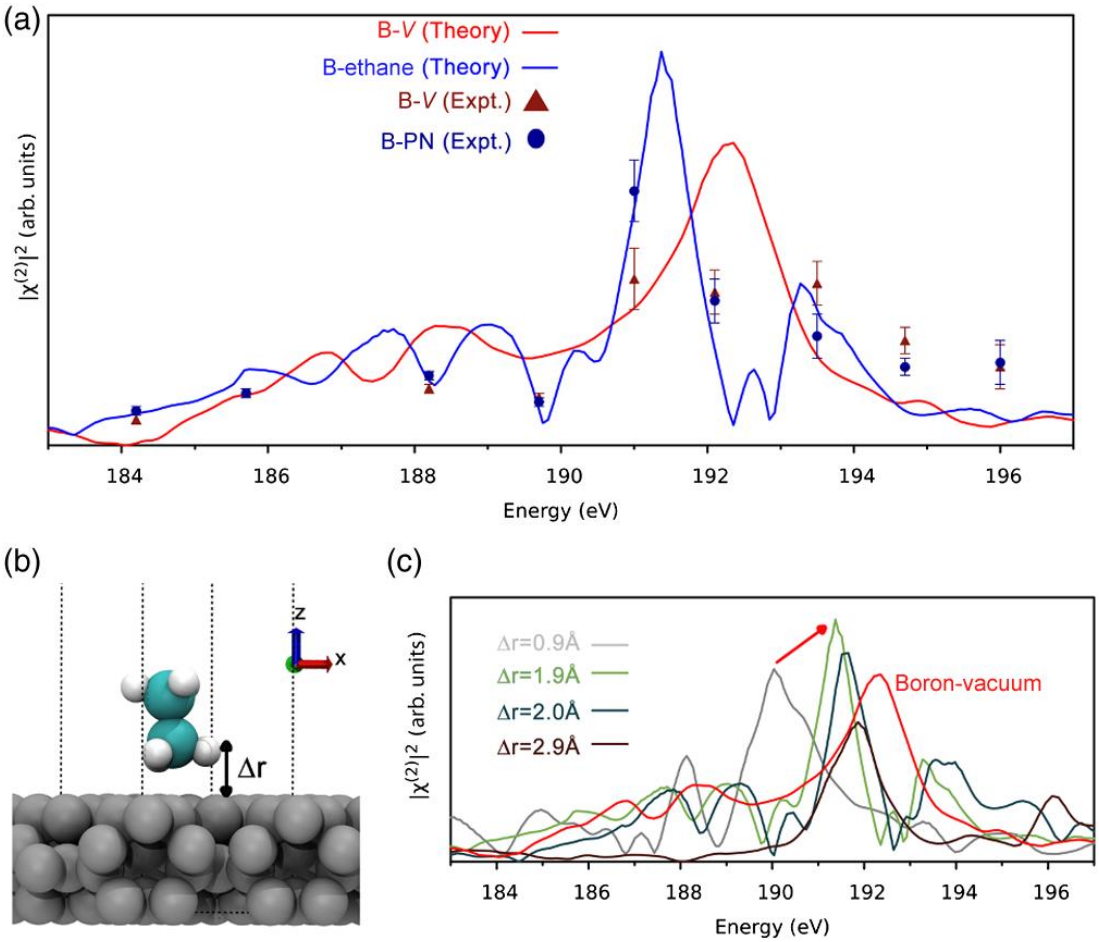

Figure. 3.3. (a) Comparison of theoretical calculations of SXR SHG boron-vacuum (red line) spectra and boron-ethane spectra (blue) at its equilibrium distance 1.9 Å with the experimental SXR SHG measurements of B-V (dark red triangles) and B-PN (dark blue circles). The calculation captures the enhancement of and the blueshift in the 191 eV feature in B-PN compared to B-V. (b) Schematic of boron-ethane computational unit cell. We vary the Δr distance between the hydrogen atom and the surface of boron. (c) Comparison of theoretical SXR SHG as a function of distance between boron and ethane, ranging from 0.9 Å (dark blue), 1.9 Å, 2.0 Å, to 2.9 Å (light blue), with the color growing increasingly light with increasing distance. As distance between the boron and ethane is increased, the primary peak at 191 eV redshifts in energy (indicated by the red arrow).

In contrast to SXR SHG results, there are no major differences in the linear TEY spectra of the two materials (Fig. 3.2). The TEY spectra are essentially identical for both samples, indicating that this technique is insufficiently sensitive to the interface to capture the differences seen in the present SXR SHG spectra. It should be noted that it is

possible for some SXR SHG signal to be generated at the back B-V interface, but this contribution will be smaller than that of the front interface due to absorption of the fundamental by the boron layer. More specifically, and as we show, the SXR SHG signal is relevant for analysis at energies above the linear absorption edge, and we operate in direct resonance of the 1s to 2p transition (K edge). The attenuation length for X rays above the edge is approximately 50 nm. Therefore, the FEL beam is largely absorbed in the boron film and the remaining intensity on the rear side is expected to have negligible contribution to the SXR SHG signal. In contrast, the generated SXR SHG signal (368 to 392 eV) from the front side is well above the B absorption edge and is therefore only weakly absorbed by the boron slab. Additionally, the back B-V interface is the same for both samples, and so will not affect any qualitative comparisons between the two interfaces. The Parylene N transmits over 90% in the photon energy ranges used here. First principles electronic structure calculations via perturbation theory within density functional theory [16,48,49] were employed to simulate the SHG response function. Here, the B-V SHG calculation was performed using two layers of boron icosahedral unit cells. In order to understand the influence of the organic molecule on the electronic structure and resulting SXR SHG spectra at the interface, we use boron-ethane (B-E) as a proxy for B-PN for computational feasibility, since both B-E and B-PN have a similar calculated line shape (Supplemental Material, Fig. S7 [26]). Given resonant conditions, the second harmonic signal in this energy range is expected to arise primarily from the top boron layer[13], such that the difference between one layer and multiple layers of ethane in the simulation is negligible. Our electronic structure calculations reveal a redshift of the SXR SHG spectrum at the boron K edge for B-E, as compared to B-V [Fig. 3.3(a)]. This

is in general agreement with the experimental spectra for B-PN vs B-V, where we find a redshift of less than 2 eV of the main SXR SHG peak at 191 eV. Although for the larger calculation we were forced to use B-E for computational reasons, the differences were small as compared to B-PN[26–41]. We explored the effect of the interfacial bond length between boron and the organic layer on the simulated spectra in Fig. 3.3(b), where we find a monotonic redshift in the 191 eV peak with increasing ethane separation, such that an increase in the separation distance from 0.9 to 1.9 Å resulted in a 2 eV shift, while a further increase to 2.9 Å lead to a further 1 eV shift. This shift is assigned to London dispersion forces as no other strong interactions are present. However, the exact spectral calculations are not quantitative because broadening, inaccuracies of the atomic positions, fluctuations in the molecular motions due to thermal energy, and the calculated spectral ringing are not accurately represented. A separation distance of 1.9 Å agrees with the minimum energy distance based upon a relaxation within DFT and is a good match to the experimental SHG spectrum. Of note, an increase in the separation distance from 1.9 to 2.0 Å resulted in a 200 meV spectral shift. As 200 meV is easily resolvable at x-ray FELs, the ability to determine distances with a resolution of 0.1 Å using this computation method has been shown previously, particularly in the bulk [16,42]. This predicted high sensitivity of SXR SHG to interfacial bond length indicates a unique and general technique for elucidating interfacial structure, but due to the low spectral density such a high accuracy cannot be obtained here. Our calculations reveal that ethane induces a shift in the Hartree potential near the interface due to electronic screening, the magnitude of which is strongly dependent on the proximity of the ethane layer to the boron surface. Density of states calculations (Fig. S10[26]) indicate that the boron core

energy levels lie at lower energy in B-E compared to B-V as a result of this screening. Thus, the experimental spectral differences between B-V and B-PN can be attributed to electronic screening in the interfacial boron atoms, rather than to specific interactions, e.g., orbital hybridization.

In conclusion, linear XAS spectra of the B-V and B-PN samples exhibited no observable difference between the two samples, whereas SXR SHG reveals distinct differences due to its sensitivity to the interface. This is the first time that a buried interface can be resolved with atom-specific sensitivity. More generally, these experiments clearly demonstrate the sensitivity of SXR SHG to subtle changes in the interfacial electronic structure of the buried interface with sensitivity to a single atomic layer. The results show that SXR SHG is highly sensitive to interfacial bond lengths and to subångstrom bond length changes, resulting in measurable spectral shifts in the hundreds of milli-electron volt range. Under the assumption of comparability of an ethane-boron interfacial bond with a Parylene N–boron interfacial bond, it was possible to determine the bond length to be approximately 1.9 Å. However, the fact that ethane had to be used as a proxy for Parylene N in simulations of varying distance highlights the importance of developing numerical methods to enable computation of larger systems with high fidelity. While SXR SHG spectroscopy clearly is a unique and powerful new tool, profound understanding of interfacial electrodynamics will require a carefully orchestrated duet of theory and experiment. Because of the ultrafast nature of the probe and its sensitivity to single atomic layers, the technique has great potential for future studies of dynamics of buried interfaces in electrochemical cells and catalysts. In the near future, SXR SHG spectroscopy can be used to probe the interfacial electronic

structure in a variety of other systems of critical interest, including electronics, batteries, and photocatalytic systems that are difficult to study with other methods. Moreover, the newly revealed high sensitivity to interfacial bond lengths and symmetries will enable unique studies on interfacial strain and its influence on electronic transport properties.

3.4. Acknowledgement

Chapter 3, in full, is a reprint of the material as it appears in Phys. Rev. Lett. 127, 096801, Craig P. Schwartz, Sumana L. Raj, Sasawat Jamnuch, Chris J. Hull, Paolo Miotti, Royce K. Lam, Dennis Nordlund, Can B. Uzundal, Chaitanya Das Pemmaraju, Riccardo Mincigrucci, Laura Foglia, Alberto Simoncig, Marcello Coreno, Claudio Masciovecchio, Luca Giannessi, Luca Poletto, Emiliano Principi, Michael Zuerch, Tod A. Pascal, Walter S. Drisdell, and Richard J. Saykally. The dissertation author was the primary investigator of the theoretical part and author of this paper. Craig P. Schwartz, Sumana L. Raj and Sasawat Jamnuch have equal contributions to the work.

3.5. Chapter 3 References

[1] H. Hong, R. D. Aburano, D.-S. Lin, H. Chen, T.-C. Chiang, P. Zschack, and E. D. Specht, X-Ray Scattering Study of Ag/Si(111) Buried Interface Structures, Phys. Rev. Lett. 68, 507 (1992).

[2] E. Gann, A. Watson, J. R. Tumbleston, J. Cochran, H. Yan, C. Wang, J. Seok, M. Chabinyc, and H. Ade, Topographic measurement of buried thin-film interfaces using a grazing resonant soft x-ray scattering technique, Phys. Rev. B 90, 245421 (2014).

[3] N. Shibata, S. D. Findlay, S. Azuma, T. Mizoguchi, T. Yamamoto, and Y. Ikuhara, Atomic-scale imaging of individual dopant atoms in a buried interface, Nat. Mater. 8, 654 (2009).

[4] P. Han, A. R. Kurland, A. N. Giordano, S. U. Nanayakkara, M.M. Blake, C.M. Pochas, and P. S. Weiss, Heads and tails: Simultaneous exposed and buried interface imaging of monolayers, ACS Nano 3, 3115 (2009).

[5] J. C. Conboy, J. L. Daschbach, and G. L. Richmond, Total internal reflection second-harmonic generation: Probing the alkane water interface, Appl. Phys. A 59, 623 (1994).

[6] J. C. Conboy and G. L. Richmond, Examination of the electrochemical interface between two immiscible electro- lyte solutions by second harmonic generation, J. Phys. Chem. B 101, 983 (1997).

[7] A.M. Jubb, D. Verreault, R. Posner, L. J. Criscenti, L. E. Katz, and H. C. Allen, Sulfate adsorption at the buried hematite/solution interface investigated using total internal reflection (TIR)-Raman spectroscopy, J. Colloid Interface Sci. 400, 140 (2013).

[8] C. T. Williams and D. A. Beattie, Probing buried interfaces with non-linear optical spectroscopy, Surf. Sci. 500, 545 (2002).

[9] A. J. Hopkins, C. L. McFearin, and G. L. Richmond, Investigations of the solid-aqueous interface with vibrational sum-frequency spectroscopy, Curr. Opin. Solid State Mater. Sci. 9, 19 (2005).

[10] G. Lüpke, Characterization of semiconductor interfaces by second-harmonic generation, Surf. Sci. Rep. 35, 75 (1999).

[11] H. Chang, P. E. Ohno, Y. Liu, E. H. Lozier, N. Dalchand, and F.M. Geiger, Direct measurement of charge reversal on lipid bilayers using heterodyne-detected second harmonic generation spectroscopy, J. Phys. Chem. B 124, 641 (2020).

[12] M. Xiao, T. Lu, T. Lin, J. S. Andre, and Z. Chen, Understanding molecular structures of buried interfaces in halide perovskite photovoltaic devices nondestructively

with sub-monolayer sensitivity using sum frequency generation vibrational spectroscopy, Adv. Energy Mater. 10, 1903053 (2020).

[13] E. Allaria et al., Highly coherent and stable pulses from the FERMI seeded free-electron laser in the extreme ultraviolet, Nat. Photonics 6, 699 (2012).

[14] E. Allaria et al., Two-stage seeded soft-x-ray free-electron laser, Nat. Photonics 7, 913 (2013).

[15] N. Rohringer, D. Ryan, R. A. London, M. Purvis, F. Albert, J. Dunn, J. D. Bozek, C. Bostedt, A. Graf, R. Hill, S. P. Hau-Riege, and J. J. Rocca, Atomic inner-shell x-ray laser at 1.46 nanometres pumped by an x-ray free-electron laser, Nature (London) 481, 488 (2012).

[16] R. K. Lam et al., Soft X-Ray Second Harmonic Generation as an Interfacial Probe, Phys. Rev. Lett. 120, 023901 (2018).

[17] Sh. Yamamoto et al., Element Selectivity in Second-Harmonic Generation of $GaFeO_3$ by a Soft-X-Ray Free-Electron Laser, Phys. Rev. Lett. 120, 223902 (2018).

[18] A. J. Achkar, T. Z. Regier, H. Wadati, Y.-J. Kim, H. Zhang, and D. G. Hawthorn, Bulk sensitive x-ray absorption spectroscopy free of self-absorption effects, Phys. Rev. B 83, 081106(R) (2011).

[19] N. Ottosson, M. Faubel, S. E. Bradforth, P. Jungwirth, and B. Winter, Photoelectron spectroscopy of liquid water and aqueous solution: Electron effective attenuation lengths and emission-angle anisotropy, J. Electron Spectrosc. Relat. Phenom. 177, 60 (2010).

[20] M. P. Seah and W. A. Dench, Quantitative electron spectroscopy of surfaces: A standard data base for electron inelastic mean free paths in solids, Surf. Interface Anal. 1, 2 (1979).

[21] S. Hüfner, Photoelectron Spectroscopy: Principles and Applications (Springer, Berlin, New York, 1996).

[22] B. H. Frazer, B. Gilbert, B. R. Sonderegger, and G. De Stasio, The probing depth of total electron yield in the sub KeV range: TEY-XAS and X-PEEM, Surf. Sci. 537, 161 (2003).

[23] M. Abbate, J. B. Goedkoop, F. M. F. de Groot, M. Grioni, J. C. Fuggle, S. Hofmann, H. Petersen, and M. Sacchi, Probing depth of soft x-ray absorption spectroscopy measured in total-electron-yield mode, Surf. Interface Anal. 18, 65 (1992).

[24] T. E. Glover, D.M. Fritz, M. Cammarata, T. K. Allison, S. Coh, J. M. Feldkamp, H. Lemke, D. Zhu, Y. Feng, R. N. Coffee, M. Fuchs, S. Ghimire, J. Chen, S. Shwartz, D. A. Reis, S. E. Harris, and J. B. Hastings, X-ray and optical wave mixing, Nature (London) 488, 603 (2012).

[25] S. Shwartz, M. Fuchs, J. B. Hastings, Y. Inubushi, T. Ishikawa, T. Katayama, D. A. Reis, T. Sato, K. Tono, M. Yabashi, S. Yudovich, and S. E. Harris, X-Ray Second Harmonic Generation, Phys. Rev. Lett. 112, 163901 (2014).

[26] See Supplemental Material at http://link.aps.org/supplemental/10.1103/PhysRevLett.000.000000 for materials and methods, detailed experimental and theoretical work including analysis of the difference between ethane and parylene N, which includes Refs. [27–42].

[27] L. Poletto, F. Frassetto, P. Miotti, A. Di Cicco, P. Finetti, C. Grazioli, F. Iesari, A. Kivimäki, S. Stagira, and M. Coreno, Spectrometer for X-ray emission experiments at FERMI free-electron-laser, Rev. Sci. Instrum. 85, 103112 (2014).

[28] G.-R. Yang, Y.-P. Zhao, J. M. Neirynck, S. P. Murarka, and R. J. Gutmann,

Chemical-mechanical polishing of polymer films: Comparison of benzocyclobutene (BCB) and parylene-N films by XPS and AFM, MRS Online Proc. Libr. 476 (1997).

[29] M. A. Barstow, M. Lewis, and R. Petre, Linear absorption coefficient of beryllium in the 50–300-Å wavelength range, J. Opt. Soc. Am. 73, 1220 (1983).

[30] S. V. Gasilov, A. Ya. Faenov, T. A. Pikuz, I. Yu. Skobelev, F. Calegari, C. Vozzi, M. Nisoli, G. Sansone, G. Valentini, S. de Silvestri, and S. Stagira, Phase-contrast imaging of nanostructures by soft x rays from a femtosecond-laser plasma, Sov. J. Exp. Theor. Phys. Lett. 87, 238 (2008).

[31] W. F. Beach, A model for the vapor deposition polymerization of p-xylylene, Macromolecules 11, 72 (1978).

[32] S. Ganguli, H. Agrawal, B. Wang, J. F. McDonald, T.-M. Lu, G.-R. Yang, and W. N. Gill, Improved growth and thermal stability of parylene films, J. Vac. Sci. Technol. A 15, 3138 (1997).

[33] W. Kohn and L. J. Sham, Self-consistent equations including exchange and correlation effects, Phys. Rev. 140, A1133 (1965).

[34] P. Hohenberg and W. Kohn, Inhomogeneous electron gas, Phys. Rev. 136, B864 (1964).

[35] A. K. Rappe, C. J. Casewit, K. S. Colwell, W. A. Goddard, and W.M. Skiff, UFF, a full periodic table force field for molecular mechanics and molecular dynamics simulations, J. Am. Chem. Soc. 114, 10024 (1992).

[36] J. Hutter, M. Iannuzzi, F. Schiffmann, and J. VandeVondele, CP2K: Atomistic simulations of condensed matter systems, WIREs Comput. Mol. Sci. 4, 15 (2014).

[37] J. P. Perdew and A. Zunger, Self-interaction correction to density-functional

approximations for many-electron systems, Phys. Rev. B 23, 5048 (1981).

[38] P. Prieto, C. Quirós, E. Elizalde, and J.M. Sanz, Electron inelastic mean free path and dielectric properties of a-boron, a-carbon, and their nitrides as determined by quantitative analysis of reflection electron energy loss spectroscopy, J. Vac. Sci. Technol. A 24, 396 (2006).

[39] N. Bloembergen, R. K. Chang, S. S. Jha, and C. H. Lee, Optical second-harmonic generation in reflection TPDELfrom media with inversion symmetry, Phys. Rev. 174, 813 (1968).

[40] C. B. Uzundal et al., Polarization-resolved extreme ultraviolet second harmonic generation from $LiNbO_3$ arXiv: 2104.01313.

[41] L. Bengtsson, Dipole correction for surface supercell calculations, Phys. Rev. B 59, 12301 (1999).

[42] E. Berger et al., Direct observation of symmetry-breaking in a ferroelectric polar metal, arXiv:2010.03134.

[43] C. Masciovecchio et al., EIS: The Scattering Beamline at FERMI, J. Synchrotron Radiat. 22, 553 (2015).

[44] A. Majhi, M. Nayak, P. C. Pradhan, E. O. Filatova, A. Sokolov, and F. Schäfers, Soft x-ray reflection spectroscopy for nano-scaled layered structure materials, Sci. Rep. 8, 15724 (2018).

[45] L. J. Terminello, G. D. Waddill, and J. G. Tobin, High resolution photoabsorption and circular polarization measurements on the University of California/National Laboratory spherical grating monochromator beamline, Nucl. Instrum. Methods Phys. Res., Sect. A 319, 271 (1992).

[46] K. G. Tirsell and V. P. Karpenko, A general purpose sub-KeV X-ray facility at the Stanford Synchrotron Radiation Laboratory, Nucl. Instrum. Methods Phys. Res., Sect. A 291, 511 (1990).

[47] M. Zangrando, D. Cocco, C. Fava, S. Gerusina, R. Gobessi, N. Mahne, E. Mazzucco, L. Raimondi, L. Rumiz, and C. Svetina, Recent results of PADReS, the photon analysis delivery and reduction system, from the FERMI FEL commissioning and user operations, J. Synchrotron Radiat. 22, 565 (2015).

[48] S. Sharma and C. Ambrosch-Draxl, Second-harmonic optical response from first principles, Phys. Scr. T109, 128 (2004).

[49] A. Gulans, S. Kontur, C. Meisenbichler, D. Nabok, P. Pavone, S. Rigamonti, S. Sagmeister, U. Werner, and C. Draxl, Exciting: A full-potential all-electron package implementing density-functional theory and many-body perturbation theory, J. Phys. Condens. Matter 26, 363202 (2014).

CHAPTER 4

Probing Lithium Mobility at a Solid Electrolyte Surface

4.1. **Abstract**

Understanding the fundamental atomic-level dynamics of lithium-ions at interfaces is of critical importance for rational design of more efficient energy storage technologies. Current lithium electrolytes in batteries composed of lithium salts dissolved in organic solvents pose safety concerns,[1,2] while side reactions and dendrite formation between the electrolyte and electrode surface greatly reduce lifetime and overall efficiency.[1] Solid-state electrolytes overcome many of these challenges, while introducing advantages including increased power, higher energy density, and increased stability of performance with changing temperatures.[3–6] However, detailed understanding of the involved lithium dynamics and chemistry is currently missing, due to a lack of direct in operando access with chemical specificity. Here, we investigate a prototypical solid-state electrolyte material and obtain insights into the surface morphology using linear and nonlinear absorption spectroscopies in the extreme ultraviolet regime. Due to its surface sensitivity, we obtained a direct spectral signature of the surface lithium ions using extreme ultraviolet second harmonic generation spectroscopy (XUV-SHG), showing a distinct spectral blue-shift, as compared to bulk absorption spectra. First-principles simulations revealed that the shift is due to transitions from the lithium 1s state into hybridized Li-s/Ti-d orbitals at the surface. Our calculations also suggest a reduction in lithium interfacial mobility due to suppressed low frequency rattling modes. This high surface resistance is common in solid-state batteries and we show that this suppression of low frequency modes is the fundamental origin of the large interfacial resistance in this material. Therefore, through interfacial engineering, we anticipate that these results

will lead to optimization strategies for general improvement of the performance of these electrochemical devices.

4.2. **Introduction**

Lithium lanthanum titanium oxide ($Li_{3x}La_{2/3-x}TiO_3$ – LLTO) is classified as a ABO_3 perovskite material (A = Li, La ; B = Ti) (see Fig. 4.1a), and consists of an alternating arrangement of La-rich and La-poor layers (or equivalently, lithium vacancy-poor and rich layers).[7,8] It is known to have one of the highest ionic conductivities for Li-ion containing oxides (1×10-3 S/cm) comparable to liquid electrolytes, and can participate in fast Li+ ion transport.[9–11] Challenges for effective application of this class of solid-state electrolytes come from limitations in physical contact, interfacial impedances, instability to contact with lithium metal and mechanical stabilization due to issues like material fractures and impurities.[5,12–15] With transition to oxide electrolyte films with thicknesses close to the range for lithium-ion battery separators these challenges may become even more pronounced, further placing attention on the chemo-electro-mechanics phenomena at the interfaces[16]. A better knowledge of the surface and interface characteristics is thus necessary to aid in determining material compositions and material designs that can effectively overcome these limitations, ultimately improving battery performance. However, to date, there are no experimental techniques that can directly probe the interface of these complex materials with atomic resolution. Thus, mechanistic understanding of the behavior of lithium ions at the interface can only be inferred from traditional electrochemical measurements employing idealized equivalent circuit models.[17,18] Extreme ultraviolet second harmonic generation (XUV-SHG) can be used to retrieve spectral signatures that specifically contain the contribution of ions at complex

interfaces. Second harmonic generation occurs when two light waves of frequency ω, called the fundamental, mix to produce a wave at twice the frequency, 2ω (Fig. 4.1b). The SHG intensity is proportional to the square of the light intensity and the second-order susceptibility $\chi^{(2)}$, where $\chi^{(2)}$ contains information related to the dielectric environment.[19] In addition, under the electric dipole approximation, the second-order susceptibility is only non-zero for systems lacking inversion symmetry, allowing SHG to probe the surface characteristics of a material exhibiting inversion symmetry in bulk as is the case in LLTO. The generally small second-order susceptibility renders the generation and detection of SHG difficult, requiring intense laser sources. Measurements in the XUV and soft X-ray regime are particularly attractive, as they enable elemental selectivity,[20,21] and have been achieved at free-electron lasers (FELs), where soft X-ray and XUV-SHG has been successfully employed to study surfaces,[19,22] and bulk anisotropies.[23–26] In addition, XUV-SHG with a tightly focused table-top source has recently been reported.[27] To understand how specific Li surface and interfacial structures can impact ion transport at LLTO surfaces, in this work we experimentally compare surface-specific properties of LLTO probed by XUV-SHG to bulk properties probed by X-ray absorption spectroscopy (XAS). Similar to XUV-SHG, XAS probes transitions between occupied and unoccupied states, providing information about the local atomic and electronic structure of Li within the material, but with the bulk signal dominating the response.[28] By comparing the features at ω of the XAS spectrum to features at 2ω in the XUV-SHG spectrum, keeping in mind the differing transitions that would occur governed by the selection rules of these two processes, differences in the bulk and surface characteristics can be determined. Spectral shifts at the Lithium K-edge

for both techniques are observed and interpreted using first-principles electronic structure simulations. Further ab initio molecular dynamics simulations reveal that the lithium dynamics are significantly suppressed at the surface due to symmetry breaking, resulting in reduced lithium entropy and mobility that are visible in the XUV-SHG, and hence the large interfacial resistance in this material.

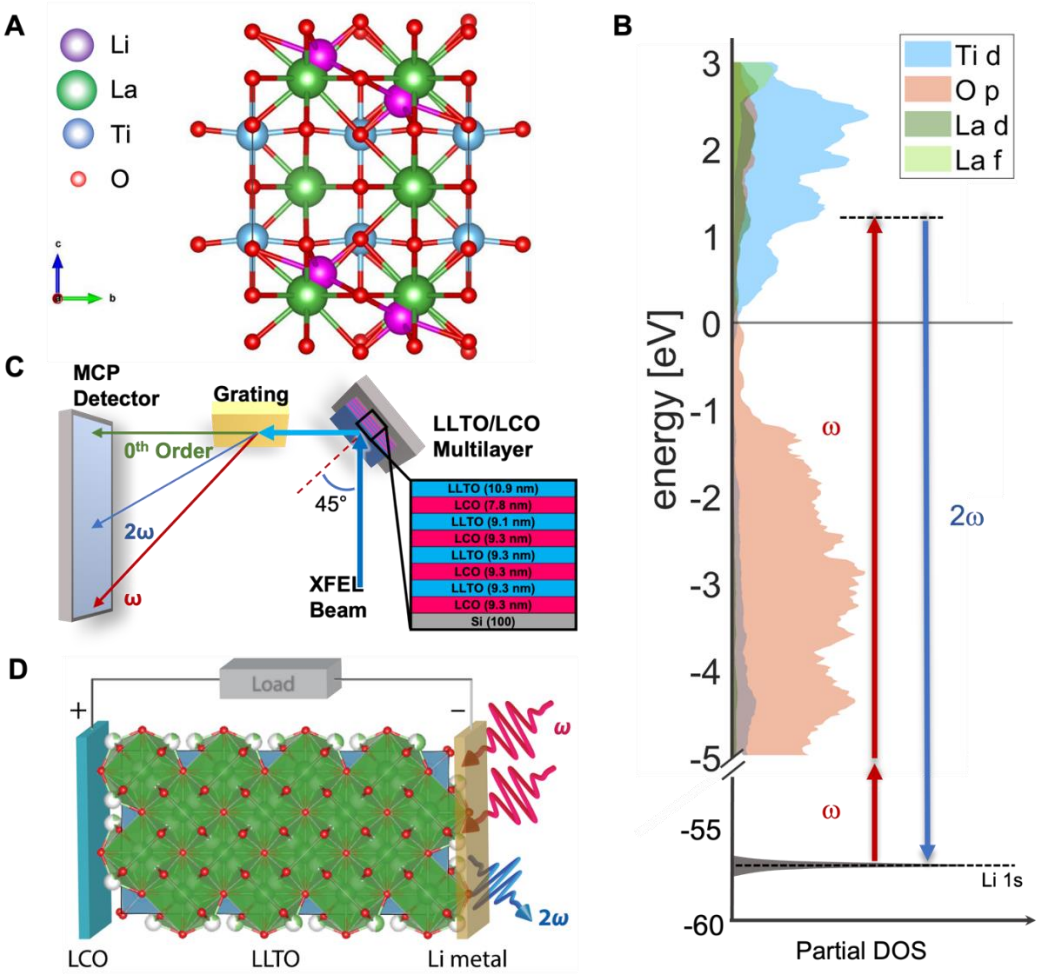

Figure 4.1. LLTO structure and experimental geometry. A, Basic crystal structure of LLTO consisting of alternating Li rich and poor layers, as well as the Ti and O octahedra. **B**, Calculated partial density of states for LLTO and indicated transitions for the XUV-SHG probe. **C**, Overview of the experimental setup used for measuring XUV-SHG data in reflection geometry. The inset shows the layered sample structure with repeating layers of LLTO and LCO. **D**, Schematic representation of an LCO-LLTO stack forming a prototypical battery with the XUV-SHG process indicated on the top surface; note that LLTO is amorphous in the film measured despite the schematic representation.

4.3. **Results and Discussion**

The sample considered here consists of alternating layers of LLTO and lithium-cobalt-oxide (LCO) (Fig. 4.1c) to represent a model solid-state battery (Fig. 4.1d). LCO is one of the most commercially successful cathode materials, while LLTO is a widely used electrolyte[29]. The bulk absorption spectra in the XUV range were retrieved from linear XUV reflectivity measurements, and contain contributions from both LLTO and LCO. The surface spectra on the same sample were measured using XUV-SHG. The thickness of the top-most LLTO layer (~11 nm) prevents access to the first buried interface of the polycrystalline LLTO-LCO stack using XUV-SHG. The discussion and analysis in this work are focused on the bulk and surface of the top layer LLTO, relevant for describing the anode (Lithium metal)/electrolyte interface (see Supplementary Sections S1–S5 for additional discussion). For selectively addressing the lithium ions and measuring the surface spectrum, the FEL is tuned across the lithium K edge (61.3 eV) at half-resonance in the range of 29 to 33 eV. The intensity of the fundamental FEL pulse $I(\omega)$ and the second harmonic signal $I(2\omega)$ are simultaneously recorded using an imaging spectrometer.

We find that the bulk linear absorption spectrum peaks at approximately 61.5 eV and monotonically decays with an increasing energy (Fig. 4.2a). By contrast, the $\chi^{(2)}(2\omega)$ spectrum features a peak around 64 eV (Fig. 4.2b). Due to the selection rules governing the SHG process, which can be viewed as the product of two dipole-allowed transitions: a Li $1s \rightarrow np \rightarrow (n+1)s/d$ (Ref. 30), it is expected that lithium 1s core electrons only have allowed transitions to unoccupied Li s final states, which may be hybridized with transition metal d states. It is also expected that the valence band is occupied and thus

not available for transitions. We confirm these hypotheses by performing first-principles, velocity-gauge real-time time-dependent density functional theory calculations[31,32] with a numerical atomic orbital basis set in order to propagate the electronic structure of LLTO under an intense laser field (see Supplementary Section S6 for details). Our calculated spectrum is in excellent agreement with the experiments. Specifically, the first low intensity feature on the XUV-SHG at 60 eV is due to transitions to Li 2s surface states that are delocalized due to hybridization with unoccupied Ti 3d-states (Fig. 2c and Figs. S6-7). Similarly, the main XUV-SHG peak at 64 eV is due to transitions to Li 3s states, but have higher intensity due to greater overlap between the core-excited state and the Lithium 1s orbital (Fig. 4.2d). We underscore that the ~ 2 eV blue shift in the XUV-SHG spectrum is due to the inherent physics of the techniques, where the XUV-SHG selection rules prohibit transitions to the unoccupied Li p states available to XAS, instead of the dichotomy between surface and bulk properties. Indeed, our simulations indicate that were it be possible to measure, the XAS of the LLTO surface would be 0.2 eV red-shifted compared to the bulk spectrum (Fig. S8).

Previous reports have shown that the X-ray XUV spectrum is very sensitive to local chemical environment and bonding chemistry.[22] Thus, the low variance in our experimental XUV-SHG spectrum and the excellent agreement with simulations, where we used a DFT relaxed static structure, indicates that the lithium mobility at the surface is significantly restricted. We test this hypothesis by means of further ab-initio simulations. First, we find that the barrier for Li migration from one lanthanum-titanium-oxygen (LTO) cage to another is significantly higher at the surface than in the bulk (Fig. 4.3a). Nudged elastic band calculations reveal a barrier for Li diffusion, which follows a

curved path that avoids empty A sites, of ~ 0.2 eV in the bulk, in good agreement with previous results[33–35]. This barrier increases to nearly 1 eV near the surface. Moreover, ab-initio molecular dynamics simulations at 298 K reveal that the Li mobility within the LTO cage is significantly more confined at the surface than in the bulk (Figs. S9 – S12). In particular, the phonon vibrational density of states (vDoS) of the surface Lithium atoms shows a depopulation of modes from 50 – 150 cm-1 (0.67 – 0.22 ps) compared to the bulk (Fig. 3b). Further analysis of the LLTO vDOS reveals that, in the bulk, the Li motions are strongly coupled with LLTO cage vibrations (Fig. 4.3c–g). For example, we find several normal modes that affect lithium mobility, primarily: (i) a mode at 62 cm-1 due to the TiO3 octahedra rotation (Fig. 4.3c), (ii) various optical modes (near 70 cm-1 and 89 cm-1 respectively) due to La displacement (Fig. 4.3d, e), and (iii) a combined La/TiO3 breathing mode near 132 cm-1 (Fig. 4.3f) (also see Supplementary Videos 1–4). At the surface, due to inversion symmetry breaking, several of these lattice vibrations are either suppressed or shifted to higher frequencies, such as cage mode E and F in Fig. 4.3g. The suppression of vibrational modes at material surface, while not a widely explored phenomena, has been observed at various clays36. From the Debye theory of solids, 37 the entropy is inversely proportional to the exponential of the frequency, so that a blue shift of the vDoS at the surface corresponds to lower entropy. Quantitatively, the suppression and blue-shift of the low frequency modes at the surface of LLTO lead to a calculated entropy of Li atom of 18.1 J/mol/K, ~40% lower than the bulk value. Our findings provide a first crucial step towards long sought-after probes for monitoring of lithium interfacial dynamics in operando. In particular, the calculated decrease in Li surface mobility and conductivity based on atomic simulations, which are consistent

with spectroscopic measurements, motivates future studies aimed at probing more complex interfaces, such as LLTO/LCO, and presently provides a rational basis for understanding one of the main obstacles facing this class of solid-state electrolytes. LLTO is known to have high grain boundary resistance,[9,38] and difficulties of achieving high interfacial mobility impedes the total ionic conductivity and effective use in batteries. It is commonly assumed that the increased interfacial impedance results from the formation of a highly disordered interphase layer at the contact point between LLTO and the electrode[29]. With this in mind, various methods of reducing the interfacial impedance have been investigated, including surface coating,[39,40] buffer layer introductions[41] and interface softening.[42] Our current results, suggesting reductions in lithium interfacial mobility at the surface due to intrinsic changes in the LLTO cage vibrational modes, provide an additional design principle. We envision future optimization strategies based on manipulation of the surface phonon modes, possibly through interface engineering and characterization of interfacial morphology by XUV-SHG. Such an approach will present a powerful new paradigm for enhancing the properties of complex material interfaces in general, which is complementary to other interface and surface sensitive spectroscopic approaches.

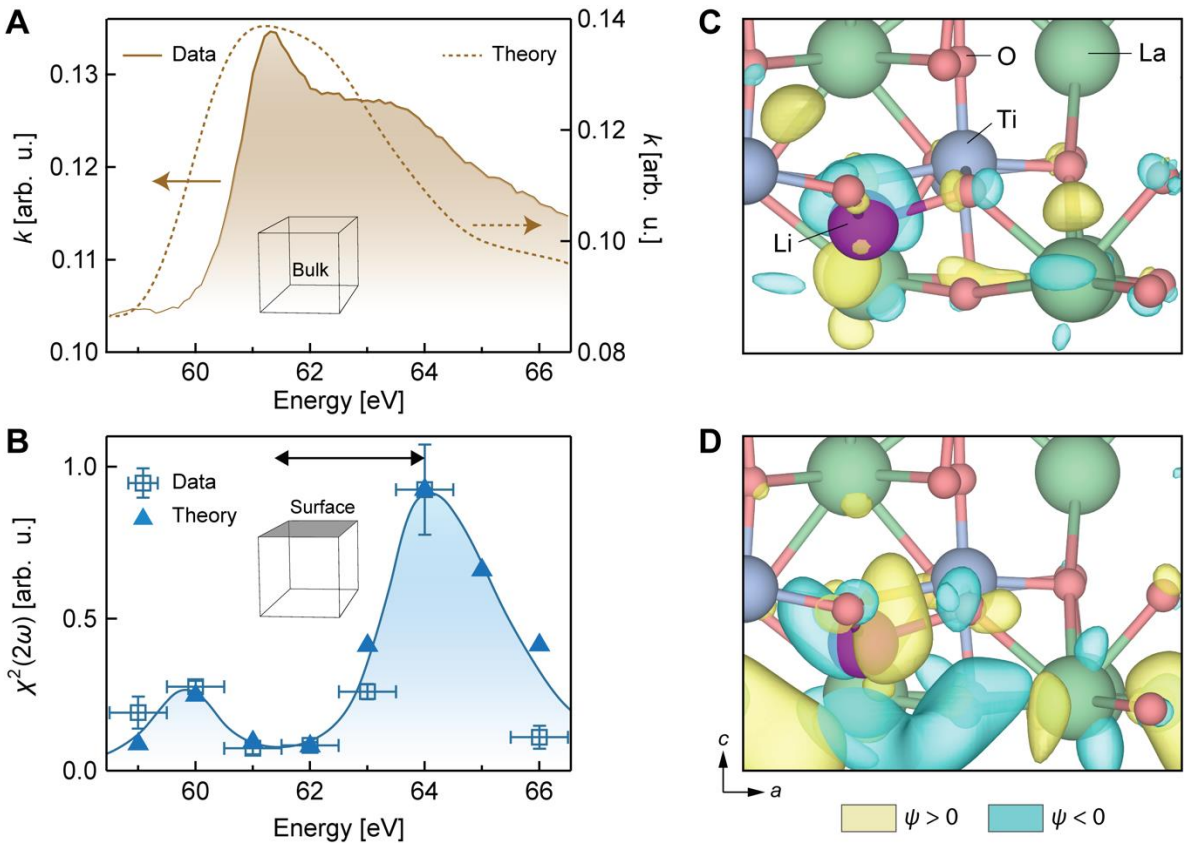

Figure 4.2. Measured and numerically simulated linear and nonlinear response of LLTO at the lithium K edge. A, The measured imaginary part of the refractive index of LLTO (brown shaded area, left axis) agrees well with the numerically retrieved linear response (dotted brown line, right axis) around the Li K-edge that appears around 61 eV in LLTO. The calculated curve is an equal-weight linear superposition of response from both LLTO and LCO. See Supplementary Figure S13 for the effect of including the LCO contribution. The slight disagreement of the linear response at higher energies could stem from broadening due to sample structure that is not existing in the simulation where an ideal crystal geometry is assumed. **B,** Experimentally derived second-order nonlinear susceptibility $\chi^{(2)}(2\omega)$ response across the Li K-edge (blue open square, blue solid line to guide the eye). The computational simulated second-order nonlinear susceptibility $\chi^{(2)}(2\omega)$ for a LLTO at the surface is shown in solid triangles in good agreement with the measurements. Vertical error bars correspond to errors in the quadratic fit of the second order response, whereas horizontal error bars are a result of energy jitter of the FEL. The double-sided arrow highlights the difference in peak positions between linear absorption (panel **A**) and second harmonic response (panel **B**). **C & D,** Representative wave function of the resulting Lithium atom core-excited states in the XUV-SHG spectrum at ~61 eV and ~64 eV, respectively. We adopt the convention that the positive phase of the wave function is colored beige while the negative phase is colored teal.

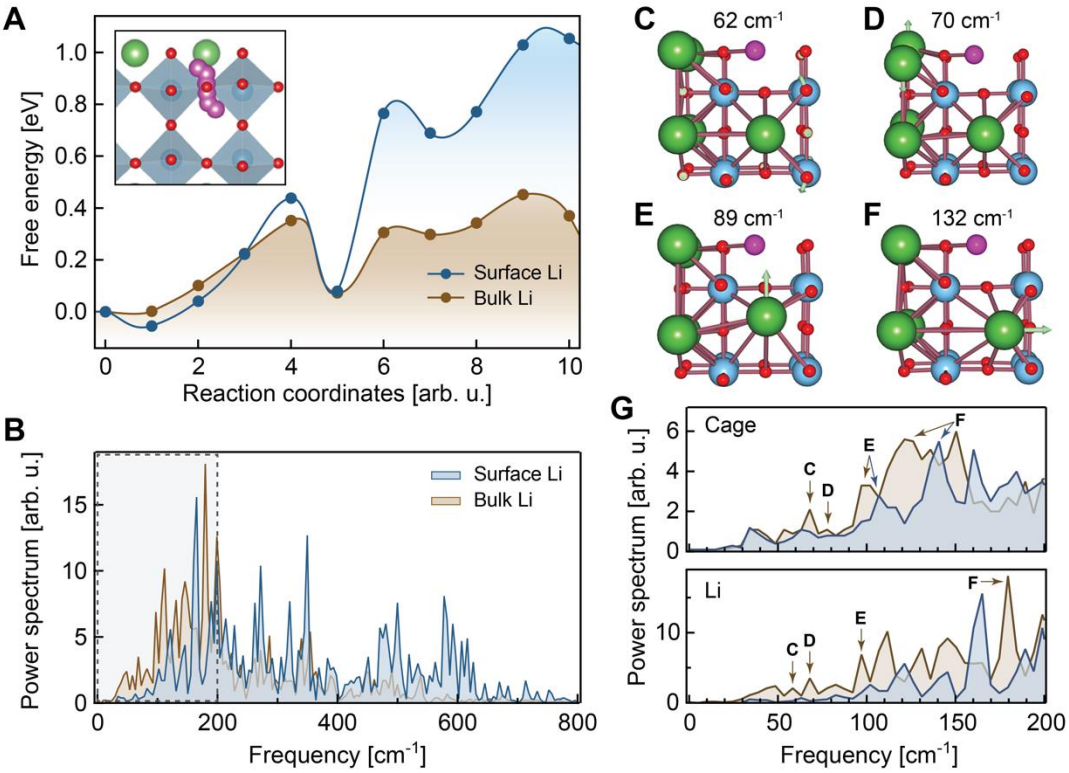

Figure 4.3. Restricted Lithium dynamics at LLTO surfaces. A, Plot of the barrier for Li migration along the low energy pathway (inset), resolved for Li atoms at the surface (blue curve) and in the bulk (brown curve). Lower barriers are calculated for bulk diffusion. **B,** Lithium vibrational density of states (vDoS) energy distribution at the surface and in the bulk LLTO. We find a reduction in the population of low frequency rattling modes from 50–100 cm^{-1}, for the surface Lithium ion, which results in a 40% reduction in the entropy. Region in the dashed rectangle is enlarged in the bottom panel of **G**. **C–F,** Visualization of the bulk LLTO vibrational modes at the indicated frequencies. The arrows indicate the general direction of the atom displacements at a particular frequency. The Li vibrational dynamics is coupled with the cage breathing modes (**C**,**F**) as well as the optical longitudinal (**D**) and traverse (**E**) modes. **G,** vDoS of the LLTO cage (*top*) and Li (*bottom*) vibrations in the low frequency range. The various vibrational modes in **C–F** are indicated. The surface cages show suppressed or blue-shifted vibrational modes, which compromises the Li interfacial dynamics.

4.4. **Methods**

Experimental methods

The XUV-SHG measurements were conducted at BL1 of the SACLA FEL43, under vacuum at ambient temperature. Data was collected using a 0.8 μm Al filter to prevent sample damage. The FEL p-polarized pulses with 30 fs pulse duration and energies ~13 μJ/pulse became incident with the LLTO-LCO multilayer at 45° relative to the surface

normal with a spot size of ~50 μm full width half maximum (FWHM). Due to the FEL beam being incident at Brewster's angle, it was heavily attenuated, with any reflectivity observed due to either polarization contamination or imperfections in beam alignment. The reflected light, consisting of the weak fundamental FEL beam and XUV-SHG signal, passes through a 200 μm horizontal slit before it is directed onto a grating 87° with respect to the surface normal. The beam was dispersed using a diffraction grating with 1200 grooves/mm before it was collected on a microchannel plate (MCP) detector (Rectangular, Hamamatsu Photonics) coated with CsI. Fundamental photon energies from the FEL were tuned from 28–33 eV in 0.5 eV steps. The resulting images were captured on a camera (IPX-VGA120-LMCN, Imperx Inc.). Shot-to-shot fluctuations of the fundamental intensity were used to retrieve the second-order susceptibility, and the slight photon energy jitter, approximately 0.2%, was used to increase the spectral resolution.

The XAS spectra were obtained from XUV reflectivity measurements that were conducted at the Lawrence Berkeley National Laboratory Advanced Light Source (ALS) at beamline 6.3.2. Details can be found in Supplementary Section S2.

Data Processing

The reflected intensity of each FEL shot was measured on the MCP detector as a two-dimensional image containing the specular reflection of the grating, fundamental (Iω) and second harmonic (I2ω) signals. At each photon energy, for a specific attenuation filter, approximately 60,000 shots were collected. After merging into a single variable, sections containing the primary features from the 2D detector image were isolated. Pixels were vertically binned and Gaussian functions were fit to the fundamental peak in

each shot. For each peak position, poor quality shots were identified as those having an r^2 value for the fit below 0.9. The outstanding shots were background corrected using the featureless portion of the spectrum that was averaged and subtracted. After initial processing, the data was merged and binned w.r.t the fundamental intensity. Within each bin, there were a sufficient number of shots used to extract the average intensity of the fundamental (Iω) peaks. The same procedure was done for the second harmonic signal within each binned spectrum. The trapezoidal rule was used to integrate over the Gaussian fit of the second harmonic signal to obtain the respective intensities. A quadratic function that was fit to the data points of (Iω) versus (I2ω) at each incident pulse energy, to extract the nonlinear susceptibility $\chi^{(2)}(2\omega)$ as a function of the photon energy. Details can be found in Supplementary Section S5.

Sample

The multilayer sample used in this study is composed of four repeating units of $Li_{3x}La_{(2/3-x)}TiO_3$ (LLTO) and $LiCoO_2$ (LCO) layers grown by pulsed laser deposition on Si(100). Using X-ray photoelectron spectroscopy (XPS) it was determined that the top layer exhibits a composition of $Li_{0.09}La_{0.64}TiO3$ and the electron density was determined by X-ray reflectivity. XPS suggests the surface may be somewhat Li-deficient, but the measured stoichiometry is reasonably consistent with the composition used for the simulations. See Supplementary Section S3 for X-ray photoelectron spectroscopy measurements and additional discussion. The top layer is LLTO, which is ~11 nm thick. See Supplementary Fig. S4 for hard X-ray reflectivity measurements that enabled determining the layer structure that is represented in the inset Fig. 4.1c.

Simulated XUV-SHG spectrum

The frequency-dependent linear response and nonlinear second harmonic susceptibility of LLTO was assessed by means of real-time velocity-gauge time dependent density functional theory[31,32]. A 2×2×2 super cell (38 total atoms) of the fundamental unit cell of LLTO perovskite structure, $Li_{0.16}La_{0.61}TiO_3$, with lattice constant a = 7.828 Å, b = 7.754 Å, c = 7.871 Å, was utilized. The electronic structure was described as a linear combination of localized atomic orbitals as implemented in the Siesta code44, using a custom double-ζ quality basis-set. The real space mesh energy cutoff was set to 5226 eV and the timestep of 0.04 a.u. (1.935 as) was used to propagate the system. The system was sampled at 5×5×5 Γ-centered k-point grid. A small impulse function is used to excite the system to extract linear response. The resulting frequency-dependent dielectric function was then obtained from Fourier transform of the current density J(t). Further details on computational methods and techniques, the reader is referred to Supplementary Sections S6-S10.

Supplementary Materials: Additional discussion and materials are provided in Supplementary Sections S1-S10 and Supplementary Figures S1-S13. Animations of the phonon modes discussed are visualized in Supplementary Videos S1-4.

4.5. **Acknowledgement**

Chapter 4, in full, is a reprint of the material submitted to Nat. Mat. with the following authors Clarisse Woodahl, Sasawat Jamnuch, Angelique Amado, Can B. Uzundal, Emma Berger, Paul Manset, Yisi Zhu, Yan Li, Dillon D. Fong, Justin G. Connell, Yasuyuki Hirata, Yuya Kubota, Shigeki Owada, Kensuke Tono, Makina Yabashi, Sanja Tepavcevic, Iwao Matsuda, Walter S. Drisdell, Craig P. Schwartz, John W. Freeland, Tod A. Pascal, Alfred Zong, Michael Zuerch. The dissertation author was the primary

investigator of the theoretical part and author of this paper. Clarisse Woodahl and Sasawat Jamnuch have equal contributions to the work.

4.6. **References**

(1) Manthiram, A. A Reflection on Lithium-Ion Battery Cathode Chemistry. Nat. Commun. 2020, 11 (1), 1550. https://doi.org/10.1038/s41467-020-15355-0.

(2) Tarascon, J.-M.; Armand, M. Issues and Challenges Facing Rechargeable Lithium Batteries. Nature 2001, 414 (6861), 359–367. https://doi.org/10.1038/35104644.

(3) Manthiram, A.; Yu, X.; Wang, S. Lithium Battery Chemistries Enabled by Solid-State Electrolytes. Nat. Rev. Mater. 2017, 2 (4), 16103. https://doi.org/10.1038/natrevmats.2016.103.

(4) Kato, Y.; Hori, S.; Saito, T.; Suzuki, K.; Hirayama, M.; Mitsui, A.; Yonemura, M.; Iba, H.; Kanno, R. High-Power All-Solid-State Batteries Using Sulfide Superionic Conductors. Nat. Energy 2016, 1 (4), 1–7. https://doi.org/10.1038/nenergy.2016.30.

(5) Quartarone, E.; Mustarelli, P. Electrolytes for Solid-State Lithium Rechargeable Batteries: Recent Advances and Perspectives. Chem. Soc. Rev. 2011, 40 (5), 2525–2540. https://doi.org/10.1039/C0CS00081G.

(6) Li, J.; Ma, C.; Chi, M.; Liang, C.; Dudney, N. J. Solid Electrolyte: The Key for High-Voltage Lithium Batteries. Adv. Energy Mater. 2015, 5 (4), 1401408. https://doi.org/10.1002/aenm.201401408.

(7) Harada, Y.; Hirakoso, Y.; Kawai, H.; Kuwano, J. Order–Disorder of the A-Site Ions and Lithium Ion Conductivity in the Perovskite Solid Solution La0.67−xLi3xTiO3 (X=0.11)11This Paper Was Presented in the 11th International Conference on SSI, Hawaii, USA, 1997. Solid State Ion. 1999, 121 (1), 245–251.

https://doi.org/10.1016/S0167-2738(99)00043-0.

(8) Okumura, T.; Ina, T.; Orikasa, Y.; Arai, H.; Uchimoto, Y.; Ogumi, Z. Effect of Average and Local Structures on Lithium Ion Conductivity in La2/3−xLi3xTiO3. J. Mater. Chem. 2011, 21 (27), 10195–10205. https://doi.org/10.1039/C0JM04372A.

(9) Ma, C.; Chen, K.; Liang, C.; Nan, C.-W.; Ishikawa, R.; More, K.; Chi, M. Atomic-Scale Origin of the Large Grain-Boundary Resistance in Perovskite Li-Ion-Conducting Solid Electrolytes. Energy Environ. Sci. 2014, 7 (5), 1638. https://doi.org/10.1039/c4ee00382a.

(10) Qian, D.; Xu, B.; Cho, H.-M.; Hatsukade, T.; Carroll, K. J.; Meng, Y. S. Lithium Lanthanum Titanium Oxides: A Fast Ionic Conductive Coating for Lithium-Ion Battery Cathodes. Chem. Mater. 2012, 24 (14), 2744–2751. https://doi.org/10.1021/cm300929r.

(11) Catti, M. First-Principles Modeling of Lithium Ordering in the LLTO (Li x La 2/3 - x /3 TiO 3) Superionic Conductor. Chem. Mater. 2007, 19 (16), 3963–3972. https://doi.org/10.1021/cm0709469.

(12) Xiao, Y.; Wang, Y.; Bo, S.-H.; Kim, J. C.; Miara, L. J.; Ceder, G. Understanding Interface Stability in Solid-State Batteries. Nat. Rev. Mater. 2020, 5 (2), 105–126. https://doi.org/10.1038/s41578-019-0157-5.

(13) Famprikis, T.; Canepa, P.; Dawson, J. A.; Islam, M. S.; Masquelier, C. Fundamentals of Inorganic Solid-State Electrolytes for Batteries. Nat. Mater. 2019, 18 (12), 1278–1291. https://doi.org/10.1038/s41563-019-0431-3.

(14) Chen, C. H.; Amine, K. Ionic Conductivity, Lithium Insertion and Extraction of Lanthanum Lithium Titanate. Solid State Ion. 2001, 144 (1), 51–57. https://doi.org/10.1016/S0167-2738(01)00884-0.

(15) Yang, K.-Y.; Leu, I.-C.; Fung, K.-Z.; Hon, M.-H.; Hsu, M.-C.; Hsiao, Y.-J.; Wang, M.-C. Mechanism of the Interfacial Reaction between Cation-Deficient La0.56Li0.33TiO3 and Metallic Lithium at Room Temperature. J. Mater. Res. 2008, 23 (7), 1813–1825. https://doi.org/10.1557/JMR.2008.0255.

(16) Balaish, M.; Gonzalez-Rosillo, J. C.; Kim, K. J.; Zhu, Y.; Hood, Z. D.; Rupp, J. L. M. Processing Thin but Robust Electrolytes for Solid-State Batteries. Nat. Energy 2021, 6 (3), 227–239. https://doi.org/10.1038/s41560-020-00759-5.

(17) Cahan, B. D.; Chen, C.-T. The Nature of the Passive Film on Iron: II . A-C Impedance Studies. J. Electrochem. Soc. 1982, 129 (3), 474. https://doi.org/10.1149/1.2123883.

(18) Shi, L.; Crow, M. L. Comparison of Ultracapacitor Electric Circuit Models. In 2008 IEEE Power and Energy Society General Meeting - Conversion and Delivery of Electrical Energy in the 21st Century; 2008; pp 1–6. https://doi.org/10.1109/PES.2008.4596576.

(19) Lam, R. K.; Raj, S. L.; Pascal, T. A.; Pemmaraju, C. D.; Foglia, L.; Simoncig, A.; Fabris, N.; Miotti, P.; Hull, C. J.; Rizzuto, A. M.; Smith, J. W.; Mincigrucci, R.; Masciovecchio, C.; Gessini, A.; Allaria, E.; De Ninno, G.; Diviacco, B.; Roussel, E.; Spampinati, S.; Penco, G.; Di Mitri, S.; Trovò, M.; Danailov, M.; Christensen, S. T.; Sokaras, D.; Weng, T.-C.; Coreno, M.; Poletto, L.; Drisdell, W. S.; Prendergast, D.; Giannessi, L.; Principi, E.; Nordlund, D.; Saykally, R. J.; Schwartz, C. P. Soft X-Ray Second Harmonic Generation as an Interfacial Probe. Phys. Rev. Lett. 2018, 120 (2), 023901. https://doi.org/10.1103/PhysRevLett.120.023901.

(20) Shen, Y. R. Surface Second Harmonic Generation: A New Technique for Surface

Studies. Annu. Rev. Mater. Sci. 1986, 16 (1), 69–86. https://doi.org/10.1146/annurev.ms.16.080186.000441.

(21) Giordmaine, J. A. Mixing of Light Beams in Crystals. Phys. Rev. Lett. 1962, 8 (1), 19–20. https://doi.org/10.1103/PhysRevLett.8.19.

(22) Schwartz, C. P.; Raj, S. L.; Jamnuch, S.; Hull, C. J.; Miotti, P.; Lam, R. K.; Nordlund, D.; Uzundal, C. B.; Das Pemmaraju, C.; Mincigrucci, R.; Foglia, L.; Simoncig, A.; Coreno, M.; Masciovecchio, C.; Giannessi, L.; Poletto, L.; Principi, E.; Zuerch, M.; Pascal, T. A.; Drisdell, W. S.; Saykally, R. J. Angstrom-Resolved Interfacial Structure in Buried Organic-Inorganic Junctions. Phys. Rev. Lett. 2021, 127 (9), 096801. https://doi.org/10.1103/PhysRevLett.127.096801.

(23) Shwartz, S.; Fuchs, M.; Hastings, J. B.; Inubushi, Y.; Ishikawa, T.; Katayama, T.; Reis, D. A.; Sato, T.; Tono, K.; Yabashi, M.; Yudovich, S.; Harris, S. E. X-Ray Second Harmonic Generation. Phys. Rev. Lett. 2014, 112 (16), 163901. https://doi.org/10.1103/PhysRevLett.112.163901.

(24) Yamamoto, S.; Omi, T.; Akai, H.; Kubota, Y.; Takahashi, Y.; Suzuki, Y.; Hirata, Y.; Yamamoto, K.; Yukawa, R.; Horiba, K.; Yumoto, H.; Koyama, T.; Ohashi, H.; Owada, S.; Tono, K.; Yabashi, M.; Shigemasa, E.; Yamamoto, S.; Kotsugi, M.; Wadati, H.; Kumigashira, H.; Arima, T.; Shin, S.; Matsuda, I. Element Selectivity in Second-Harmonic Generation of GaFeO3 by a Soft-X-Ray Free-Electron Laser. Phys. Rev. Lett. 2018, 120 (22), 223902. https://doi.org/10.1103/PhysRevLett.120.223902.

(25) Berger, E.; Jamnuch, S.; Uzundal, C. B.; Woodahl, C.; Padmanabhan, H.; Amado, A.; Manset, P.; Hirata, Y.; Kubota, Y.; Owada, S.; Tono, K.; Yabashi, M.; Wang, C.; Shi, Y.; Gopalan, V.; Schwartz, C. P.; Drisdell, W. S.; Matsuda, I.; Freeland, J. W.;

Pascal, T. A.; Zuerch, M. Extreme Ultraviolet Second Harmonic Generation Spectroscopy in a Polar Metal. Nano Lett. 2021, 21 (14), 6095–6101. https://doi.org/10.1021/acs.nanolett.1c01502.

(26) Uzundal, C. B.; Jamnuch, S.; Berger, E.; Woodahl, C.; Manset, P.; Hirata, Y.; Sumi, T.; Amado, A.; Akai, H.; Kubota, Y.; Owada, S.; Tono, K.; Yabashi, M.; Freeland, J. W.; Schwartz, C. P.; Drisdell, W. S.; Matsuda, I.; Pascal, T. A.; Zong, A.; Zuerch, M. Polarization-Resolved Extreme-Ultraviolet Second-Harmonic Generation from LiNbO3. Phys. Rev. Lett. 2021, 127 (23), 237402. https://doi.org/10.1103/PhysRevLett.127.237402.

(27) Helk, T.; Berger, E.; Jamnuch, S.; Hoffmann, L.; Kabacinski, A.; Gautier, J.; Tissandier, F.; Goddet, J. P.; Chang, H.-T.; Oh, J.; Pemmaraju, C. D.; Pascal, T. A.; Sebban, S.; Spielmann, C.; Zuerch, M. Table-Top Extreme Ultraviolet Second Harmonic Generation. Sci. Adv. 2021, 7, eabe2265.

(28) Kaplan, C. J.; Kraus, P. M.; Gullikson, E. M.; Borja, L. J.; Cushing, S. K.; Zürch, M.; Chang, H.-T.; Neumark, D. M.; Leone, S. R. Retrieval of the Complex-Valued Refractive Index of Germanium near the M 4,5 Absorption Edge. J. Opt. Soc. Am. B 2019, 36 (6), 1716. https://doi.org/10.1364/JOSAB.36.001716.

(29) Gao, Z.; Sun, H.; Fu, L.; Ye, F.; Zhang, Y.; Luo, W.; Huang, Y. Promises, Challenges, and Recent Progress of Inorganic Solid-State Electrolytes for All-Solid-State Lithium Batteries. Adv. Mater. Deerfield Beach Fla 2018, 30 (17), e1705702. https://doi.org/10.1002/adma.201705702.

(30) Boyd, R. W. Nonlinear Optics; Academic Press: New York, 2008.

(31) Pemmaraju, C. D.; Vila, F. D.; Kas, J. J.; Sato, S. A.; Rehr, J. J.; Yabana, K.;

Prendergast, D. Velocity-Gauge Real-Time TDDFT within a Numerical Atomic Orbital Basis Set. Comput. Phys. Commun. 2018, 226, 30–38. https://doi.org/10.1016/j.cpc.2018.01.013.

(32) Pemmaraju, C. D. Valence and Core Excitons in Solids from Velocity-Gauge Real-Time TDDFT with Range-Separated Hybrid Functionals: An LCAO Approach. Comput. Condens. Matter 2019, 18, e00348. https://doi.org/10.1016/j.cocom.2018.e00348.

(33) Zhang, Y.; Zheng, Z.; Liu, X.; Chi, M.; Wang, Y. Fundamental Relationship of Microstructure and Ionic Conductivity of Amorphous LLTO as Solid Electrolyte Material. J. Electrochem. Soc. 2019, 166 (4), A515. https://doi.org/10.1149/2.0161904jes.

(34) Zhu, Y.; Wu, S.; Pan, Y.; Zhang, X.; Yan, Z.; Xiang, Y. Reduced Energy Barrier for Li+ Transport Across Grain Boundaries with Amorphous Domains in LLZO Thin Films. Nanoscale Res. Lett. 2020, 15 (1), 153. https://doi.org/10.1186/s11671-020-03378-x.

(35) Zheng, Z.; Zhang, Y.; Song, S.; Wang, Y. Sol–Gel-Processed Amorphous Inorganic Lithium Ion Electrolyte Thin Films: Sol Chemistry. RSC Adv. 2017, 7 (48), 30160–30165. https://doi.org/10.1039/C7RA04609J.

(36) Zeitler, T. R.; Greathouse, J. A.; Gale, J. D.; Cygan, R. T. Vibrational Analysis of Brucite Surfaces and the Development of an Improved Force Field for Molecular Simulation of Interfaces. J. Phys. Chem. C 2014, 118 (15), 7946–7953. https://doi.org/10.1021/jp411092b.

(37) McQuarrie, D. A. Statistical Mechanics; University Science Books, 2000.

(38) Knauth, P. Inorganic Solid Li Ion Conductors: An Overview. Solid State Ion. 2009, 180 (14), 911–916. https://doi.org/10.1016/j.ssi.2009.03.022.

(39) Han, X.; Gong, Y.; Fu, K. (Kelvin); He, X.; Hitz, G. T.; Dai, J.; Pearse, A.; Liu, B.; Wang, H.; Rubloff, G.; Mo, Y.; Thangadurai, V.; Wachsman, E. D.; Hu, L. Negating Interfacial Impedance in Garnet-Based Solid-State Li Metal Batteries. Nat. Mater. 2017, 16 (5), 572–579. https://doi.org/10.1038/nmat4821.

(40) Takada, K.; Ohta, N.; Zhang, L.; Xu, X.; Hang, B. T.; Ohnishi, T.; Osada, M.; Sasaki, T. Interfacial Phenomena in Solid-State Lithium Battery with Sulfide Solid Electrolyte. Solid State Ion. 2012, 225, 594–597. https://doi.org/10.1016/j.ssi.2012.01.009.

(41) Ohta, N.; Takada, K.; Sakaguchi, I.; Zhang, L.; Ma, R.; Fukuda, K.; Osada, M.; Sasaki, T. LiNbO3-Coated LiCoO2 as Cathode Material for All Solid-State Lithium Secondary Batteries. Electrochem. Commun. 2007, 9 (7), 1486–1490. https://doi.org/10.1016/j.elecom.2007.02.008.

(42) Seino, Y.; Ota, T.; Takada, K. High Rate Capabilities of All-Solid-State Lithium Secondary Batteries Using Li4Ti5O12-Coated LiNi0.8Co0.15Al0.05O2 and a Sulfide-Based Solid Electrolyte. J. Power Sources 2011, 196 (15), 6488–6492. https://doi.org/10.1016/j.jpowsour.2011.03.090.

(43) Owada, S.; Togawa, K.; Inagaki, T.; Hara, T.; Tanaka, T.; Joti, Y.; Koyama, T.; Nakajima, K.; Ohashi, H.; Senba, Y.; Togashi, T.; Tono, K.; Yamaga, M.; Yumoto, H.; Yabashi, M.; Tanaka, H.; Ishikawa, T. A Soft X-Ray Free-Electron Laser Beamline at SACLA: The Light Source, Photon Beamline and Experimental Station. J. Synchrotron Radiat. 2018, 25 (1), 282–288. https://doi.org/10.1107/S1600577517015685.

(44) Soler, J. M.; Artacho, E.; Gale, J. D.; García, A.; Junquera, J.; Ordejón, P.; Sánchez-Portal, D. The SIESTA Method for Ab Initio Order-N Materials Simulation. J. Phys. Condens. Matter 2002, 14 (11), 2745. https://doi.org/10.1088/0953-8984/14/11/302.

CHAPTER 5

Conclusion and Future Work

5.1 Summary of the Work Presented in the Dissertation and Future Work

The main goal of the research present herein was to develop theoretical framework for core electron spectroscopy second harmonic generation and provide understanding at atomic level to the experiment. Chapter 2 through 4 explored different interfaces and noncentrosymmetric material with increasing complexity to demonstrate second harmonic generation from core level electron in XUV and soft X-ray is interface probe with elemental selectivity. A brief summary of each chapter is described below.

Chapter 2 discussed the second harmonic generation in ferroelectric perovskite $LiOsO_3$ polar metal. The focus was on the Li atoms which are displaced from centrosymmetric position. The $LiOsO_3$ in polar state is shown to be second harmonic active in the optical regime. We demonstrate from the simulation that it is also the case for XUV regime response at Li 1s with sensitivity dependent on the Li displacement. The work presented here allows us to extend this technique to study material with mobile Li such as battery system.

Chapter 3 discussed the second harmonic generation at buried inorganic-organic junction. Here the boron atoms representing inorganic media in junction with parylene-N polymer are probed and compared to boron/vacuum interface. In the X-ray linear response regime, it was shown that the response is not surface sensitive and nearly identical responses are observed. Whereas, the soft X-ray second harmonic generation showed different responses which we found to be dependent on the distance between inorganic/organic junction. Our work established a possible tool at angstrom resolution to look at buried interface allowing one to effectively probe buried interface at elemental selectivity.

Chapter 4 discussed the second harmonic generation at battery solid-electrolyte lithium lanthanum titanate. The solid-electrolyte serves as a media for Li to move during battery operation. We probed the Li 1s second harmonic response and compare the properties of the Li in bulk and at the surface. The Li is found to be less favorable at the surface showing that the surface Li is relatively at higher energy. We demonstrated that the Li migration path is more difficult as it moves from the bulk toward the surface. The vibrational modes stabilizing the Li atoms are absent at the surface. Our work serves as a first ever demonstration of second harmonic generation into prototype battery material.

Future directions for this technique can be divided into two parts first being the experiment and the latter in the theoretical framework. The experiment can extend to work on different area of materials such as catalyst or multilayer heterostructure. The technique developed is universal and could be applicable to any arbitrary system. On the theory side, the implementation of higher level of theory such as inclusion of many-body effect is of interest. The improvement to the accuracy of the simulation is crucial for atomic level understanding. In addition, different computational approach to improve the efficiency of the calculation as often the simulation of interface is very computationally demanding. The future direction for this work is looking into liquid/liquid interface which is one of the most common interface for chemistry. Thus, the continued development of core electron second harmonic generation spectroscopy both in the experimental technique and theoretical framework would serve as a powerful tool for investigation of interface.